Light Water Reactor Sustainability Program

Concept for Integrated Multi-Modal Online Piping Monitoring System along with Data Fusion and Advanced Data Analytical Algorithms using High-Resolution Fiber Optics Sensors

September 2020

U.S. Department of Energy

Office of Nuclear Energy

Concept for Integrated Multi-Modal Online Piping Monitoring System along with Data Fusion and Advanced Data Analytical Algorithms Using High-Resolution Fiber Optics Sensors

Andrei Gribok, Mohan Wang, Jingyu Wu, Qirui Wang, Abhishek Venketeswaran, Kehao Zhao, and Kevin Chen

September 2020

ABSTRACT

One of the primary challenges in ensuring safe and economically viable operation of nuclear power plants (NPPs) is to develop cost-effective and robust condition-based maintenance technology. However, after several decades of operations, NPPs have often evolved into unique, complex, and difficult systems for condition-based maintenance (CBM) implementation. This research report describes our efforts in FY-19 and FY-20 to develop distributed fiber sensors that can withstand harsh NPP environments to perform high spatial resolution active measurements for plant-scale monitoring. Data harnessed by fiber sensors were analyzed using various machine learning algorithms for defect detection and pipe health prognosis. Our research in FY-20 was primarily focused on the following four aspects:

- Working with Corning Inc., we have developed a new optical fiber that is suitable for reel-to-reel sensor fabrication without a fiber draw-tower facility. Using both femtosecond laser direct writing and KrF UV excimer laser fabrication schemes, fiber sensors are now produced in optical fiber without stripping polymer jackets. This effort represents a major advancement in distributed fiber sensor technology.

- To ensure the survivability of optical fiber sensors for NPP applications, our team carried out comprehensive laser writing optimization efforts and the evaluation of high-temperature fiber sensor stability. Through laser fabrication optimization tailored for a high-temperature environment, our team demonstrated that ultra-low-loss fiber sensors can be fabricated to sustain a temperature of 800°C for long periods of times.

- Digital twin modeling, using finite element analysis (FEA), our team performed detailed numerical modeling of guided acoustic wave propagation in defective pipelines with elbow and T-junction structures. These simulation results have been compared with experimental data for mutual validation. Through both experimental data harness and numerical modeling, our team aims to use integrated data to train the neural networks developed in Year 1 to improve the efficacy of artificial intelligence.

- Through both the experimental and numerical modeling presented above, the frequency range of guided acoustic signal with significant propagation distance has been identified. Based on this knowledge, our team developed a low-cost distributed fiber sensor and interrogation system prototype that is suitable for field deployment. This work could significantly reduce the deployment cost of fiber sensors.

The success of this project will have a significant impact on the future of NPPs. It will lead to new robust distributed fiber sensors that can be applied to a wide range of NPP components and systems for a high spatial resolution data harness. The artificial intelligence big data analytics through deep learning using combined modeling and experimental data will extract critical information from sensor data, even if it is obscured by complex component shapes, structural aging, and variations due to sensor installation (human errors). This will enable accurate prognosis of plant health and the development of effective CBM strategy. The success of this project will significantly reduce operational costs, lower plant downtime, and improve compliance of regulatory requirements for both nuclear and fossil fuel power plants.

CONTENTS

FIGURES

TABLES

ACRONYMS

ϕ-OTDR	Phase-sensitive optical time-domain reflectometry
CBM	Condition-based monitoring
CNN	Convolutional neural network
DAS	Distributed acoustic sensing
DOFS	Distributed optical fiber sensor
EDFA	Erbium-doped fiber amplifier
EMI	Electromagnetic interference
FBG	Fiber Bragg Grating
FEA	Finite element analysis
FFT	Fast fourier transform
FRM	Faraday rotator mirror
GW	Guided wave
GWT	Guided wave testing
IFPI	Intrinsic Fabry-Perot Interferometer
LANL	Los Alamos National Laboratory
LBNL	Lawrence Berkeley National Laboratory
LM	Levenberg-Marquardt
MDL	Minimum description length
MLP	Multi-layer perceptron
MsS	Magnetostrictive sensor
NA	Numerical aperature
NDE	Nondestructive evaluation
NN	Neural network
NPP	Nuclear power plant
NRL	Naval Research Laboratory
OBR	Optical backscattering reflectometer
OFDR	Optical frequency domain reflectometry
OPD	Optical path length
PSD	Power spectral density
RAL	Random airline-cladding
RMSE	Root mean square error
SEM	Scanning electron microscope
SHM	Structural health monitoring

SLED	Superluminescent light emitting diode
SMV	Support vector machine
SNR	Signal-to-noise ratio
SOA	Semiconductor optical amplifier
SOM	Self-organizing map
SSC	System, structure, and component
SVD	Singular value decomposition
SwRI	Southwest Research Institute
TRL	Technology readiness level
U.S.	United States
UV	Ultraviolet
FOS	Fiber optic sensor

1.   BACKGROUND AND INTRODUCTION

This is the last of a series of reports detailing the concept for an integrated multi-modal online piping monitoring system along with data fusion and advanced data analytical algorithms using high-resolution fiber optics sensors In previous reports, our research team utilized a femtosecond point-by-point writing approach to produce high-temperature, radiation-resilient fiber sensors for distributed acoustic sensor (DAS) applications. In FY-20, the team made efforts to address challenges with laser fabrication technology to fabricate fiber sensors with high-temperature resilience for nuclear power plant (NPP) applications.

A major challenge incurred in sensing fiber fabrication is the optically opaque fiber polymer coating at ultraviolet (UV) wavelengths. The fiber polymer coating, made of acylate or polyimide, is not transparent at deep UV wavelength where photon energy of the laser is strong enough to induce refractive index change in-fiber core to produce sensors. There are two existing techniques to overcome this difficulty. The first approach, which has been applied for large-scale sensing fiber manufacturing, is the so-called "draw-tower" approach." The laser inscription of the fiber sensor is carried out directly on the fiber draw-tower using a UV laser before applying a polymer coating onto the fiber. This approach is enormously expensive and inflexible. Fabrication of every sensing fiber requires a fiber drawing operation to produce new fibers, which incurs very high costs. Currently in the United States (U.S.), OFS is the only company that is developing this capability, but it is not open for commercial use. Due to this monopoly, the Naval Research Laboratory (NRL), Los Alamos National Laboratory (LANL), and Lawrence Berkeley National Laboratory (LBNL) are developing their own versions of this capability for specialized works. Most of these sensing fibers are manufactured in Europe and Asia and sold to the world market at $50-$100/meter. The other approach is to use femtosecond laser direct writing while our research group is leading these efforts. Using the nonlinear multiphoton process, it is possible to use near infrared femtosecond laser pulse that is optically transparent to fiber coating to induce refractive index change in optical fiber core using a high numerical aperture (NA) objective. However, this approach involves precise optical alignment and could induce large optical loss at sensing points (~0.2 dB/points), which limits length of sensing fibers.

Our team worked with Corning Inc. this fiscal year to develop a new type of optical fiber that is amendable for reel-to-reel sensor fabrications without draw-towers. We will present the research accomplishments of the development of these new fibers and the fabrication of fiber sensors for both DAS and distributed temperature sensing in this report. To ensure survivability of optical fiber sensors for NPP applications, we carried out comprehensive laser writing optimization efforts and evaluation of high-temperature stability of fiber sensors. Through femtosecond laser fabrication optimization tailored for high-temperature environment, we demonstrated that ultra-low-loss fiber sensors can be fabricated to sustain 800°C temperature for long periods of time.

Also during FY-20, our data analytics research efforts were focused on a machine learning algorithm development for experimental data. In this year, we took a digital twin modeling approach to validate our experimental data. Using FEA, we performed detailed numerical modeling of guided acoustic wave propagation in defective pipelines with elbow and T-junction structures. These simulation results have been compared with experimental data for mutual validation. Through both experimental data harness and numerical modeling, we aim to use integrated data to train the neural networks we developed in FY-2019 to improve the efficacy of artificial intelligence.

Through both the experimental and numerical modeling presented above, the frequency range of guided acoustic signal with significant propagation distance has been identified. Based on this knowledge, we developed a low-cost distributed fiber sensor and interrogation system prototype suitable for field deployment. This work could significantly reduce deployment costs for fiber sensors.

In the following sections, we will detail our research efforts in these four aspects from new fiber developments to sensor fabrication, to modeling, and to sensor interrogation system developments. We believe efforts invested in Year 2 has led to strong possibilities to new technology and products with high technology readiness levels (TRLs).

2. DEVELOPMENT OF NEW OPTICAL FIBERS FOR REEL-TO-REEL LASER FABRICATIONS OF FIBER SENSORS USING UV LASERS

Rayleigh-based distributed optical fiber sensors (DOFSs) are useful for detecting changes in temperature, strain, pressure, relative humidity, chemical concentration, radiation, etc. They can find many applications in security and leak monitoring on oil and gas pipelines, intrusion detection, and for down-hole sensing in oil wells, etc. In Rayleigh scatter based distributed fiber optic sensing, a coherent laser pulse is sent along an optic fiber, and Rayleigh scattering along the fiber cause the fiber to act as a distributed interferometer with a gauge length approximately equal to the pulse length. The intensity of the reflected light is measured as a function of time after the transmission of the laser pulse. Changes in the reflected intensity of successive pulses from the same region of fiber are caused by changes in the optical path length of that section of fiber. A major limitation of Rayleigh scattering based fiber sensors is the low Rayleigh scattering intensity of conventional optical fibers. This limits the resolution and sensitivity of fiber sensors.

To address the low Rayleigh scattering problem, different approaches have been investigated. Rayleigh backscattered power can be increased by raising the numerical aperture (NA) of the fiber to increase the capture efficiency for backscattered light. However, within the practical single-mode fiber design space, the increase of capture efficiency is less than 2dB. Adding scattering particles can also increase scattering, but this approach typically increases the attenuation of the fiber. Another approach involves laser processing of optical fiber to increase the optical backscattering. It is well known that the exposure of optical fiber to pulsed radiation may increase the Rayleigh scattering. The backscattering can be increased further by forming periodic or quasi-periodic weak Bragg gratings. Such a weak Bragg grating can be applied over long fiber lengths without significantly increasing the fiber attenuation. Fabrication of gratings over a long length of fiber can be done with UV exposure during the fiber draw before the coating is applied. But aligning the laser system with the fiber during the fiber draw is difficult, especially with fiber vibration during the draw. One method requires removing the coating for UV exposure and recoating the fiber for protection. In this method, the coating applied during the fiber draw is wasted and the coating removal process may introduce defects on the glass surface that can cause fiber reliability issues. Another method uses special UV transparent coating to allow UV light to reach the fiber core. However, the special UV transparent coating is expensive and limits the fiber draw speed.

In this report, we demonstrate a new method for fabricating weak Brag grating with thin polymer coatings that is amendable for UV laser sensor fabrication without stripping fiber jackets or using a draw-tower. This type of fiber has the potential to completely reshape the distributed fiber sensor industry for distributed measurements and applications.

In a backscattering based distributed sensing system, as shown in Figure 1, a pulse with a power of P0 is launched into the fiber at z=0. At a location of z, part of the P power is reflected and reaches by the detector:

$$P_s = C\alpha_s \Delta l P_0 e^{-2\alpha z} \tag{1}$$

where α_s is the scattering coefficient, C is the capture coefficient for the scattered light, α is the loss coefficient, and Δl is the pulse sensing segment that is related to pulse width. For Rayleigh scattering based sensors, the capture efficiency:

$$C = \frac{3v_g}{k_0^2 n_{eff}^2 D_{MF}^2} \tag{2}$$

where v_g is the group velocity, n_{eff} is the effective index, k_0 is the wavenumber, and D_{MF} is the mode field diameter. Because the Rayleigh scattering coefficient of typical single-mode fiber is small, and only a fraction of the scattered light is captured by the core, the backscattered signal is low, which limits the sensing distance and sensitivity.

To increase the scattering coefficient, we propose to create weak Bragg gratings along the fiber using UV light exposure. For a Bragg grating, light is reflected when the phase matching condition is satisfied. The wavelength λ that is reflected is determined by the following equation:

$$\lambda = 2n_{eff}\Lambda \tag{3}$$

where Λ is the period of grating and n_{eff} is the effective index of the guided mode. Because the reflection by the grating is within the fiber core, the capture efficacy is about 100%. In addition, because the scattered light is only in the backward direction, the attenuation increase is much smaller than increasing the Rayleigh scattering, which happens in all directions.
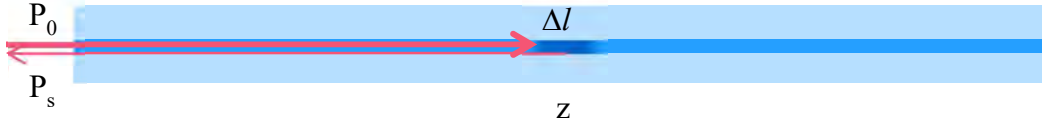
Figure 1. Backscattering based distributed sensing system schematic.

2.1   New Optical Fibers for UV Laser Sensor Fabrications

A typical fiber coating thickness with acrylate polymer materials is 62.5 μm, which is too thick to transmit UV light. To write a grating on such a fiber, the coating materials must be removed. After the grating is written, the fiber needs to be recoated to protect the glass. Or, one can use a fiber with a UV transparent coating, which is more expansive than UV curable coatings, and is difficult to apply with high draw speeds. To solve these problems, we propose to use thin-coated fibers. The thin coating allows the UV light to go through to reach the core for making gratings. At the same time, it provides adequate mechanical protection that allows the fiber to be handled for continuous grating making without fiber breaks. After the grating is made, the fiber can be coated with additional coating for more protection, or it can be cabled directly to make a sensing cable. In the following paragraphs, we describe how to make thin-coated fibers and write Bragg gratings.

The proposed fiber structures with a thin coating are shown schematically in Figure 2. Figure 2 (left) shows a fiber with a single coating, while Figure 2 (right) shows a fiber with a dual coating. The glass diameter is in the range of 100 to 125 μm (e.g., 100, 105, 110, 115, 120, 125 μm). The coating thickness is ≤ 20 μm (e.g., 2, 3, 5, 7.5, 10, 15, 20 μm). The coated fiber has a diameter ≤ 145 μm (e.g., 110, 125, 135, 145 μm. For dual coating layers, the ratio of the thickness of the primary over the secondary coating is in the range of 0.8 to 1.2. The coating material can be acrylate, polyimide (PI), polyetherimide (PEI), or any other polymer materials. Young's modulus of cured primary coating is ≤ 5 MPa (e.g., 0.5, 1, 3, 4 MPa). Young's modulus of cured secondary coating is ≥ 0.5 GPa (e.g., 1, 2, 4, 5, 8, 10 GPa). To promote adhesion between the coating and the glass, silanes or other additives can be added into a coating. The types of thin-coated fibers demonstrated in this report are listed in Table 1.

Figure 2. Single layer thin fiber coating geometry (left) and dual-layer thin fiber coating geometry (right).

Table 1. Thin-coated fibers fabricated and experimented.

Fiber Type	Fiber ID	Description(Clad/Coat)
Reduced Clad, Acrylate Coating	121-6599-301	125μm/132um
	121-6599-401	125um/140um
Reduced Clad, Polyimide Coating	PI-2574	133um/137um
	121-6602-c#121-6589-5	140um/142um
Reduced Clad, PEI Coating	WS1777	127um/129um

To improve glass mechanical strength and dynamic fatigue properties, a Titania doped glass strengthen layer can be added to the glass surface. Compressive stress is formed in the Titania doped glass layer, which strengthens the cladding surface in a similar manner as the Gorilla Glass. In addition, the formation of microcrystals due to doping of Titania may stop defects such as scratches from propagating through the fiber, resulting further fatigue resistance. The doping concentration of Titania of the Titania layer is 5-25%. The thickness of the Titania layer is in the range from 1–20 μm, as long as it does not interfere with the index profile of the fiber core, which causing leaky loss of light from the core to the cladding. The fiber index profile may be a standard single-mode fiber, a bend insensitive single-mode fiber, a few mode fiber, or a multimode fiber.

2.2   UV Laser Sensor Fabrications Results

The UV laser Bragg grating fabrication setup is schematized in Figure 3(a). The thin-coated fiber was tested to inscribe ultra-weak Fiber Bragg Grating (FBG) by an KrF 248nm laser using a chirped phase mask. The incident beam was first normalized by a UV beam expander (CVI Laser Optics, BXUV) and then focused by a cylindrical lens (CVI Laser Optics, SCX-C) with a focal length of 40 mm along the fiber core. The focused light shone through a phase mask and the diffractive radiation after the phase mask was split into zero and plus/minus one order. The fiber is positioned directly behind the phase mask. The interference pattern on the fiber formed by two beams of plus and minus one order was used to imprint the fringe patterns on fiber core. The alignment of thin-coated fiber and the phase mask is shown in Figure 3(c). The focused beam size on the fiber is about 4 cm × 300 μm. An Erbium broadband source (MPB Technologies Inc, EBS-7210) and an optical spectrum analyzer (OSA) (Agilent, 86140B) were deployed to characterize the reflected spectrum of the written FBG. A circulator was used to obtain the reflected light. The reflection was detected and measured by the OSA. A 4 cm-long uniform Bragg grating with Bragg wavelength at ~1550 nm and a 2 cm long chirped UWFBG with central Bragg wavelength at ~1550 nm exposed at different radiation intensity (from 80 mJ to 180 mJ pulse energy) were inscribed in the fiber core to characterize the performance of various types of thin-coated fibers shown in Table 1 during the experiment.
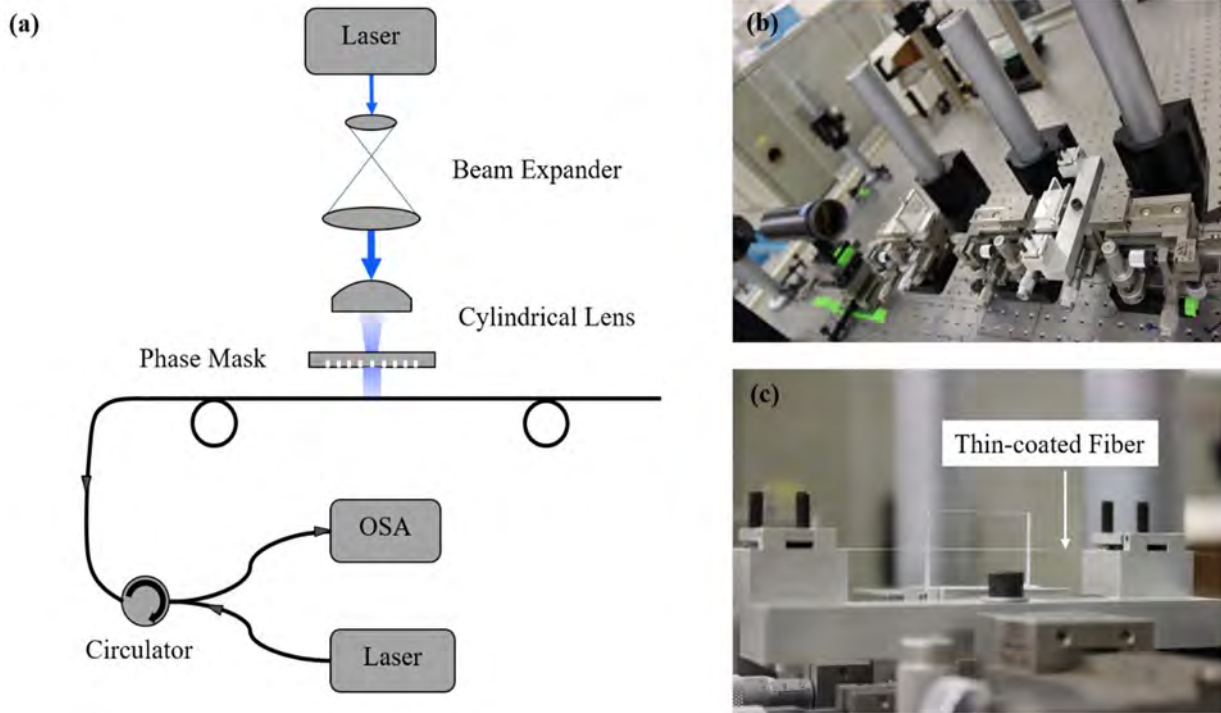
Figure 3. Fabrication setup for weak Bragg grating on thin-coated fibers.

Figure 4(a) and Figure 4(b) show the surface of the thin acrylate coated fiber with a diameter of 132 μm and 140 μm after a 10-pulse of the laser radiation at 180 mJ pulse energy (e.g., on-target pulse fluence 1.5J/cm^2). No obvious laser-induced damage can be seen on the fiber, which is demonstrated by scanning electron microscope (SEM) images captured in Figure 4. As a result, thin acylate coating is sufficiently transparent for weak FBG inscription. Fiber with a thicker coating diameter (i.e., > 140 μm) will be tested later for this project.
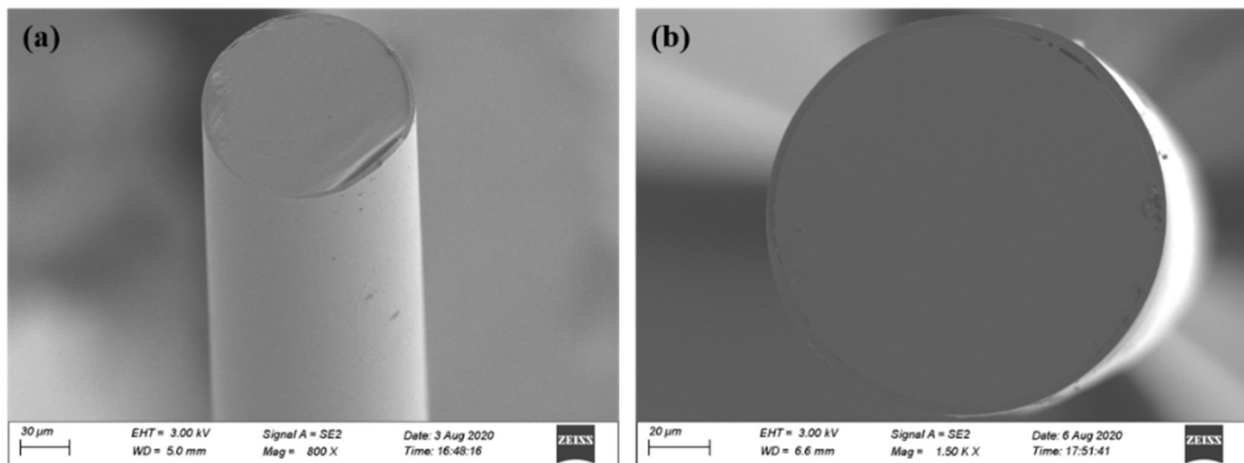
Figure 4. SEM image of (a) the cross-sectional, and (b) the side view of 132 μm thin-coated fiber after laser radiation.

Although UV laser irradiation did not produce damage on thin polymer coating made of acylate, it did induce visible damage to other type of fiber coating. For all fiber types using the KrF 248-nm pulse UV laser, the optical fiber coated with polyimide and PET polymer materials sustain damages. Figure 5

summarizes all fibers irradiated by UV lasers and the surface quality of the coating after the laser irradiation. Figure 5(a) and Figure 5(b) show optical microscope side images of fiber coated with a 3.5 μm thick acrylate coating. A comparison between fiber before and after laser irradiation shows no visible damage. This is consistent with our SEM studies shown in Figure 4. The same observation under both SEM and optical microscopes reveal that fiber with thicker acylate coating also exhibit no coating damage as shown in Figure 5(c) and Figure 5(d) for optical fiber with a 7.5 μm thick acrylate coating.

However, the laser did induce damage after a 3-pulse of laser radiation at 100-mJ pulse energy (on-target pulse fluence 0.83J/cm^2) for fiber coated with high-temperature durable polyimide and PET coating. These are obvious on thin polyimide and PEI coating, which is shown in Figure 5(f), Figure 5(h), and Figure 5(j). For fiber coated with 2 μm thick polyimide coating, the laser irradiation using the above on-target pulse fluence reduces the overall fiber diameter to 133 μm, which is the same of the diameter of the fiber without polymer coating. This suggests that the UV laser ablated away of polyimide fiber coating. This is not a surprise as polyimide is a strong UV light absorbing materials despite desirable properties of polyimide coating, such as high-temperature resilience.

No Bragg grating is formed after laser illumination for fiber coated with polyimide and PEI coating. Most UV light may be captured by the polyimide and PEI coating on the exposure to laser illumination and thus dissociates molecular bonds, resulting in photo-oxidation reaction which scissor or crosslink the polymer chains and leading to discoloration of the coating. The discoloration of the polyimide coating could be seen clearly in Figure 5(f) compared to Figure 5(e). The defect caused by UV irradiation on the fiber would degrade its properties severely. The formation of the laser-induced damage will be further investigated.

The SEM and optical microscope studies reveal that fiber coated with thin acrylate coating can have sufficient UV transparency to support reel-to-reel UV laser fabrication for distributed fiber sensors. Given the low temperature resilience of acylate materials, these fiber sensors will be useful for a wide range of distributed fiber sensor applications with operational temperature less than 100°C. With proper protection, such as adding an armor protective tube, the operational temperature can be further improved, which will be investigated in Year 3.
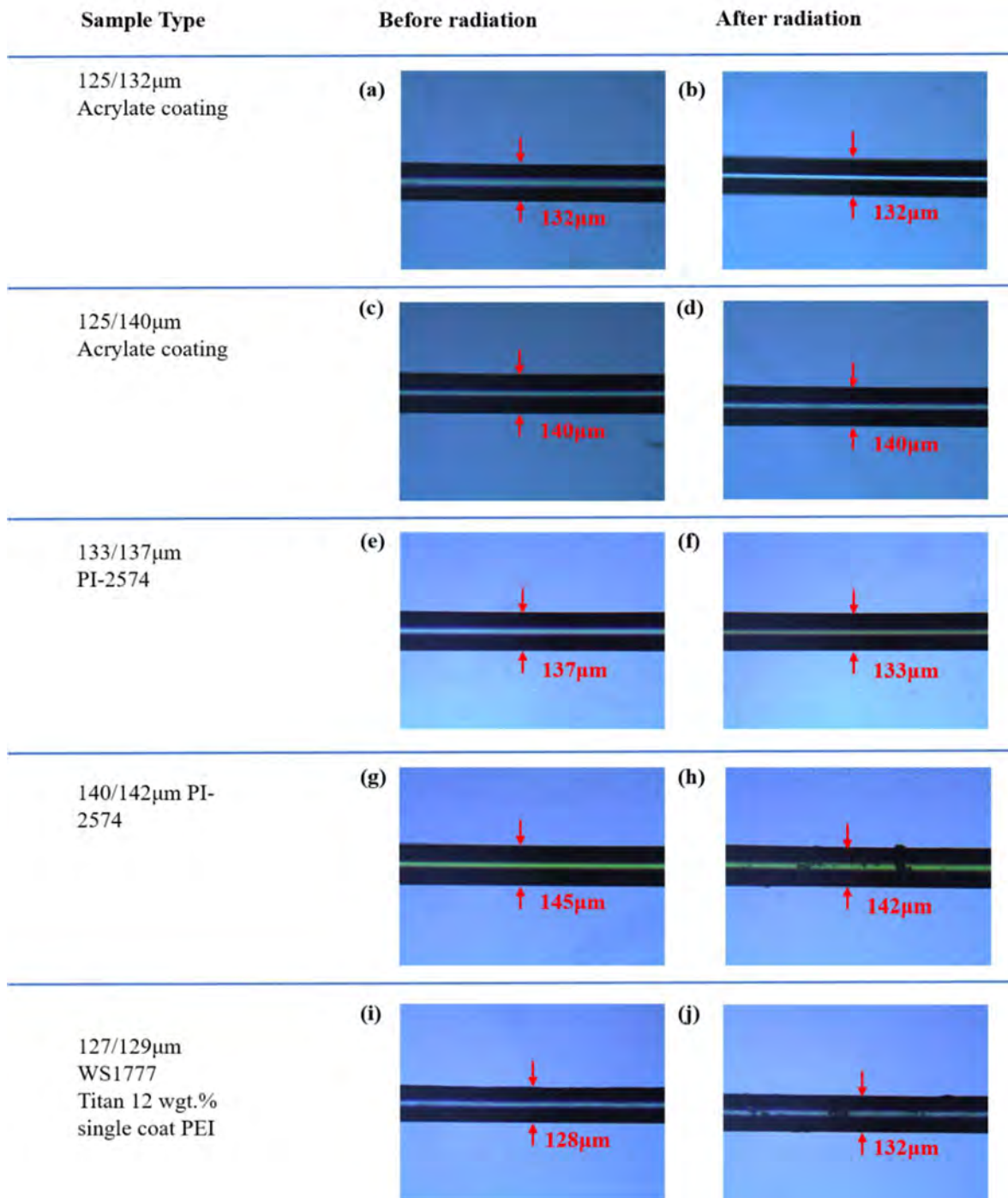
Figure 5. Optical microscopy image of various thin-coated fibers before and after laser radiation.

2.3   Uniform Weak FBG Sensors

Using a phase mask, narrow band FBG sensors are fabricated in an acylate coated fiber with a 3.5 μm and a 7.5 μm thick polymer coating. Figure 6 shows the 3.5 μm coating and Figure 7 shows the 7.5 μm coating FBG reflectance vs laser pulse numbers. As shown in Figure 5, only six pulses are sufficient to produce FBG strong enough for sensing applications. This suggests these types of fibers are full amendable for reel-to-reel distributed fiber sensors fabrications.
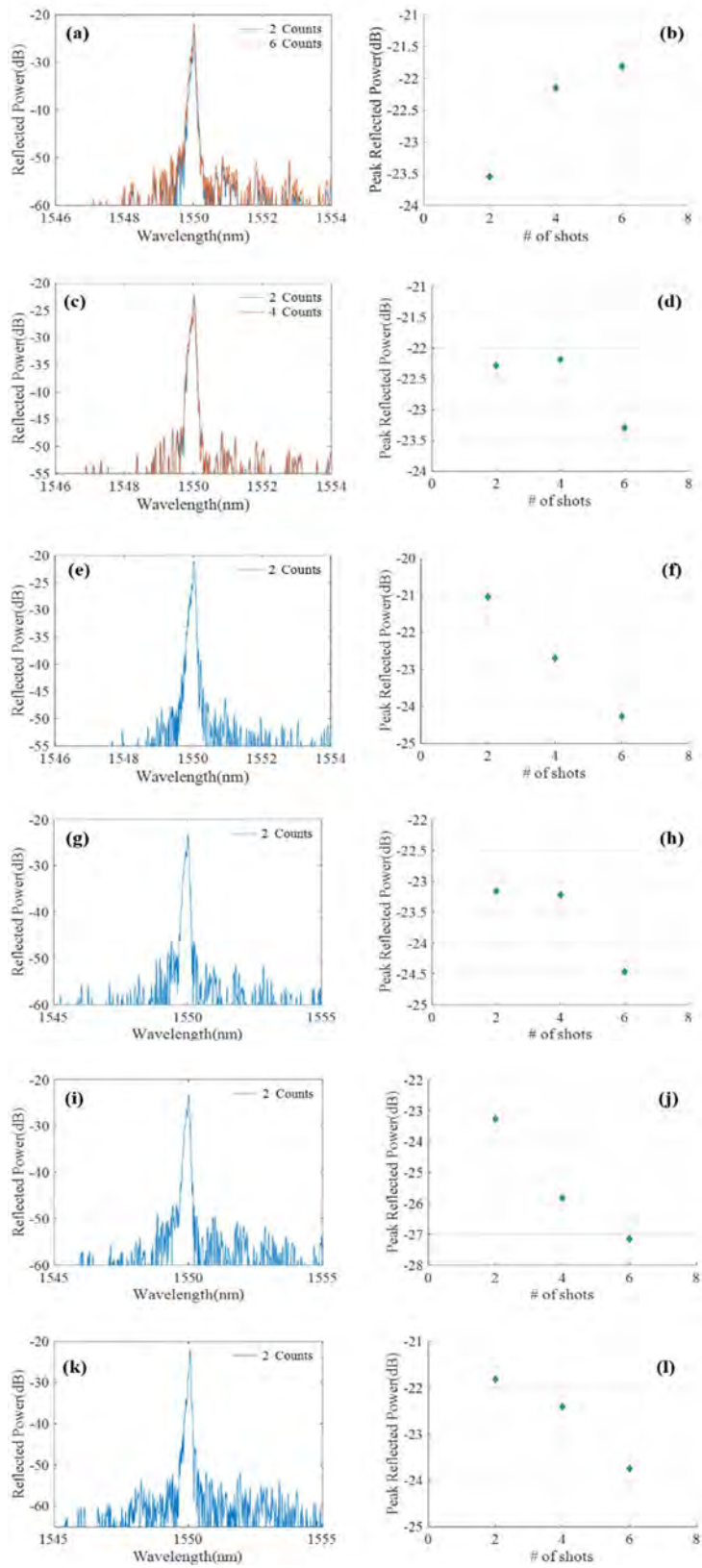
Figure 6. The reflected spectra and peak reflectance of the uniform FBG on thin-coated fiber with diameter of 132 μm after exposure of laser radiation at different pulse energy.
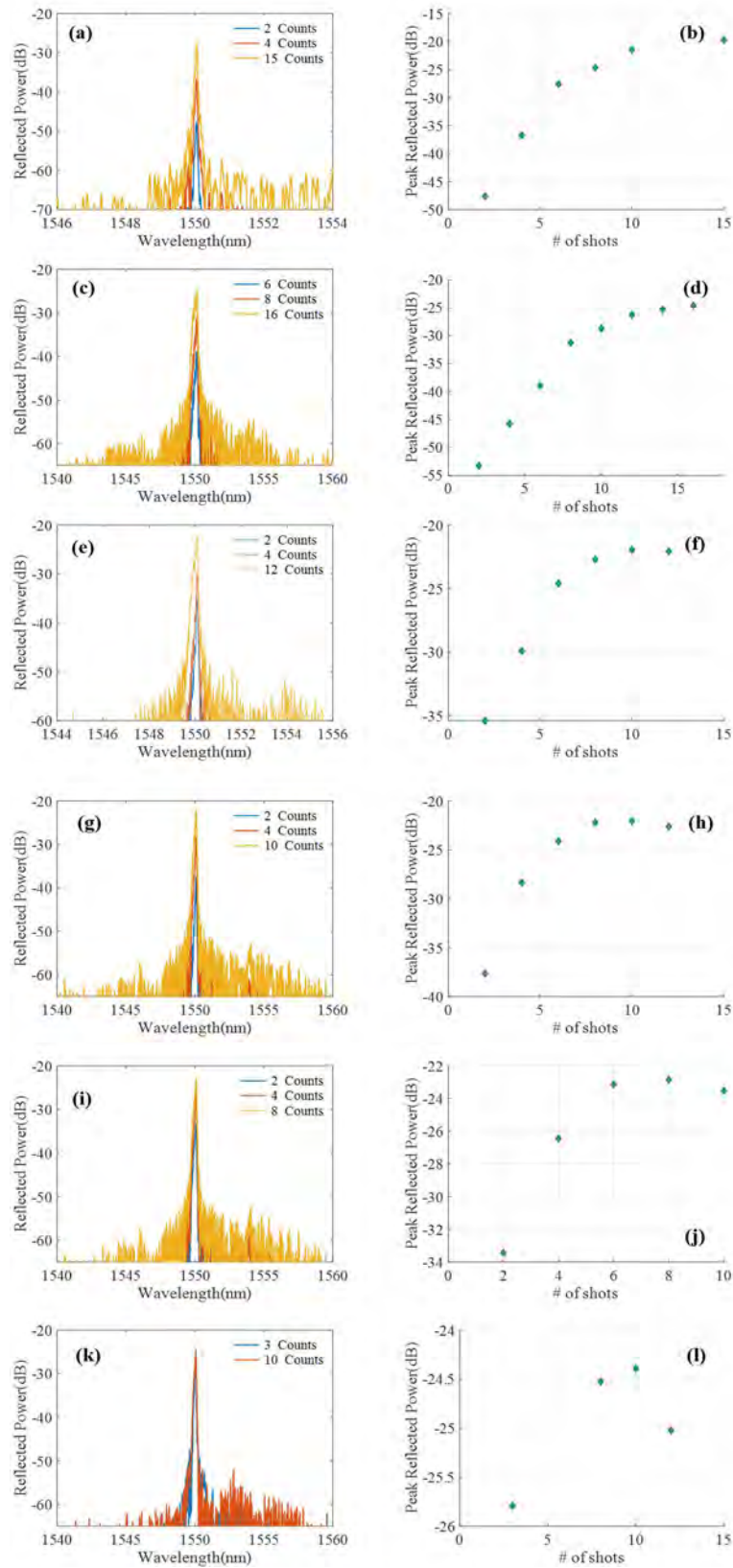
Figure 7. The reflected spectra and peak reflectance of the uniform FBG on thin-coated fiber with diameter of 140 μm after exposure of laser radiation at different pulse energy.

The reflection spectra of weak uniform FBG on thin-coated fiber with diameter of 132 μm and 140 μm shown in Figure 6 and Figure 7, respectively, were exposed to laser radiation at pulse energy, 80 mJ, 100 mJ, 120 mJ, 140 mJ, 160 mJ and 180 mJ, respectively.

The reflection spectra of weak uniform FBG on thin-coated fiber with diameter of 132 μm on the exposure from two laser shots to six shots of UV irradiation are shown in Figure 6(a), (c), (e), (g), (i), and (k) at different pulse energy levels. The reflection peak began to decrease sharply after several shots of UV illumination. For example, the Bragg peak was reduced after two shots of UV irradiation as shown in Figure 6(f). This continuous reduction in peak uniform FBG amplitude indicates thin acylate coating filters UV light and the cumulative energy produces thermal stress inside the fiber core, which might start to degrade leading to increased absorption of 248 nm laser light. Thus, no more grating could be formed on the fiber core. The threshold of the number of laser radiation shots increases as the laser illumination intensity increases. This indicates that most UV light is transmitted through the thin acrylate coating to the fiber core before the fiber is exposed to more radiation. The peak reflectivity of the uniform FBG on thin-coated fiber with a diameter of 132 μm is about 0.7049% (i.e., 180 mJ, 2 counts). The intensity of the peak reflectivity is related to the value of pulse energy. The peak amplitude of FBG is associated with the exact pulse energy and the absorption rate of UV light on the thin coating under exposure. The exact relationship between the amplitude of the peak reflectivity and pulse energy will be further investigated with more improved and repeated experiments. The reflection spectra of weak uniform FBG on thin-coated fiber with a diameter of 140 μm on the exposure from 2 to 16 shots of UV irradiation are shown in Figure 7(a), (c), (e), (g), (i), and (k) at different pulse energy levels. Similarly, the continuous increase of the peak reflectivity of weak uniform FBG stops when the fiber is exposed to more shots of UV light as shown in Figure 7(l). Generally, the highest reflectivity is obtained on exposure to ten shots of laser radiation.

The peak reflectance of 0.7049% is more than enough for fiber sensing applications. As a matter of fact, this peak reflectance is too strong for distributed fiber sensors as many applications demands multiplexing of well over 1000 FBG sensors. Based on these scenarios, a 0.05% peak reflectance will be sufficient for fiber sensing. Therefore, results presented in Figure 7 are more than sufficient for fiber sensor applications.

2.4   Chirped FBG Sensors for DAS

In addition to produce narrow linewidth fiber sensors for temperature measurements, broadband chirped FBGs were also fabricated for DAS. The reflectivity at the central Bragg wavelength on thin-coated fiber with a diameter of 132 μm as a function of laser pulse numbers from 2–4 shots are shown in Figure 8(a), (c), (e), (g), (i), and (k) at different pulse energy levels from 80 mJ to 180 mJ with an interval of 20 mJ. The peak reflectivity at central Bragg wavelength is obtained when the fiber is exposed to around four shots of UV light as shown in Figure 8(l). The peak intensity is about 0.2% at the central Bragg wavelength. As indicated in Figure 10(a), the reflectivity of the chirped FBG at 1550 nm is related to the value of pulse energy when the thin-coated fiber is exposed to the same number of shots of laser radiation. As pulse energy increases, reflectivity increases slightly except the point of 120 mJ. Figure 9 shows the similar results on thin-coated fiber with a diameter of 140 μm. The peak reflectivity at central Bragg wavelength is obtained when the fiber is exposed to around eight shots of UV light, as shown in Figure 9(l). In Figure 10(b), as the value of UV pulse energy increases, the reflectivity of the weak chirped FBG written after the same pulse shots increases. The reflectivity is the highestunder the exposure to radiation at 180 mJ pulse energy.
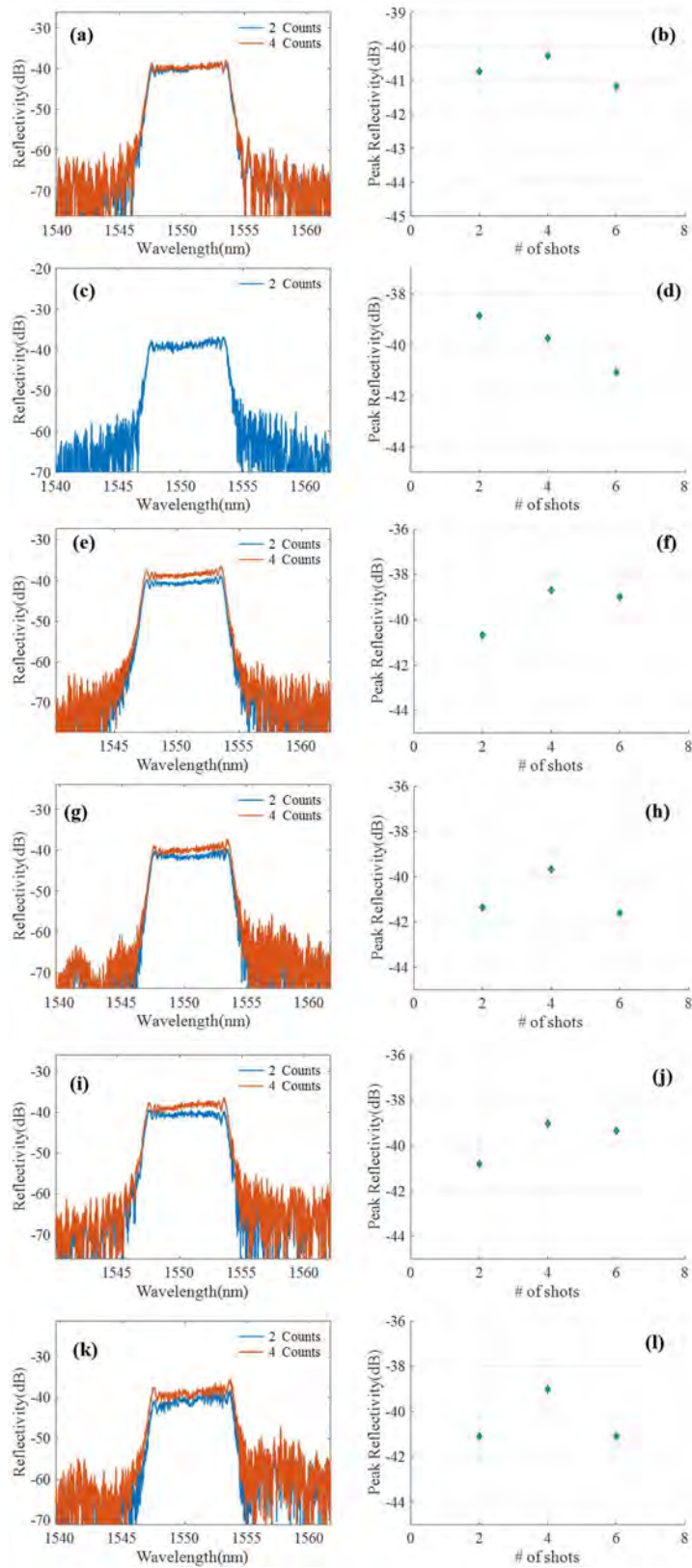
Figure 8. The reflected spectra and peak reflectance of the chirped FBG on thin-coated fiber with a diameter of 132 μm after exposure of laser radiation at different pulse energy.
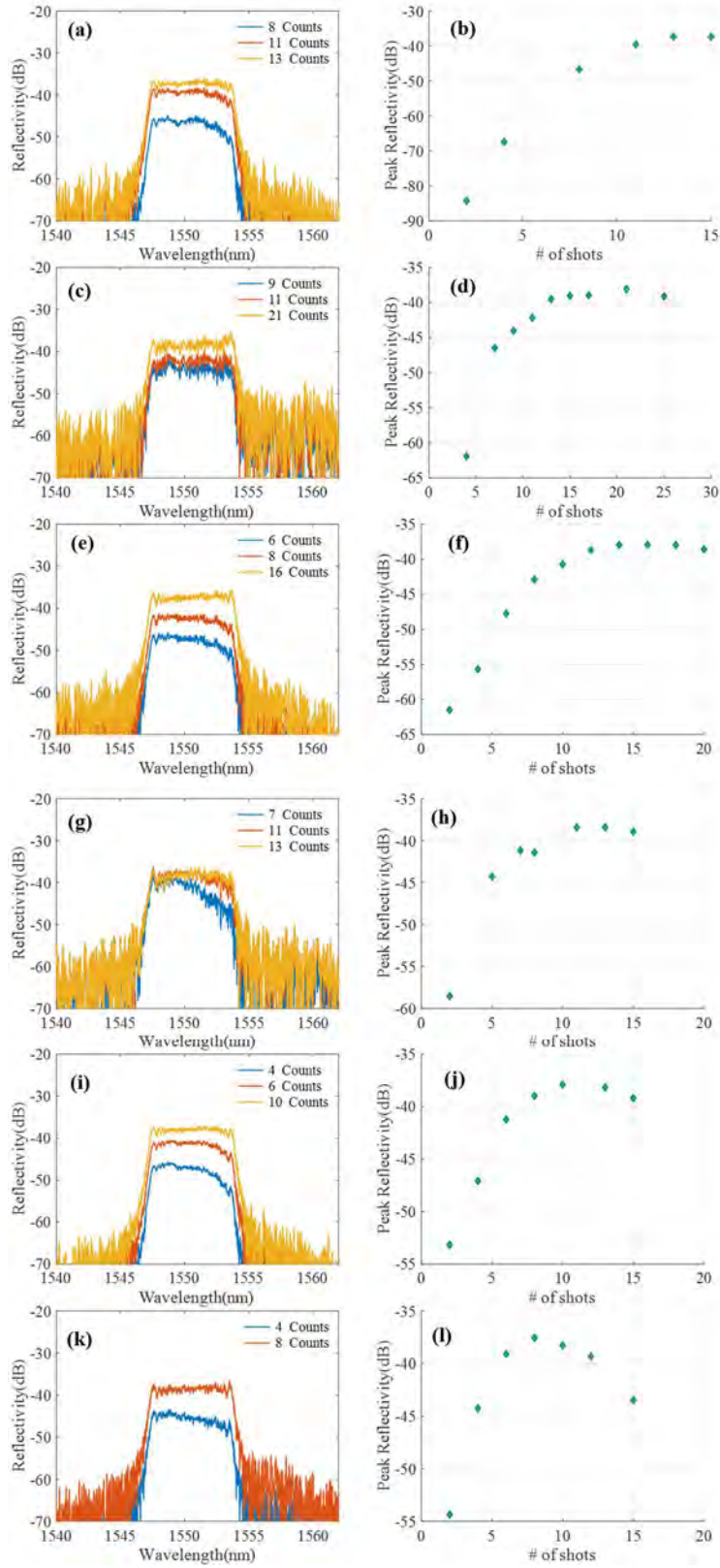
Figure 9. The reflected spectra and peak reflectance of the chirped FBG on thin-coated fiber with a diameter of 140 μm after exposure of laser radiation at different pulse energy.

Figure 10 shows preliminary results of reel-to-reel fabrication of chirped FBG array for DAS applications. Using deep UV KrF 248 nm excimer laser irradiation through a phase mask approach. A chirped FBG with 10 nm bandwidth can be produced in specialty fiber with a 3.5 μm acrylate coating.
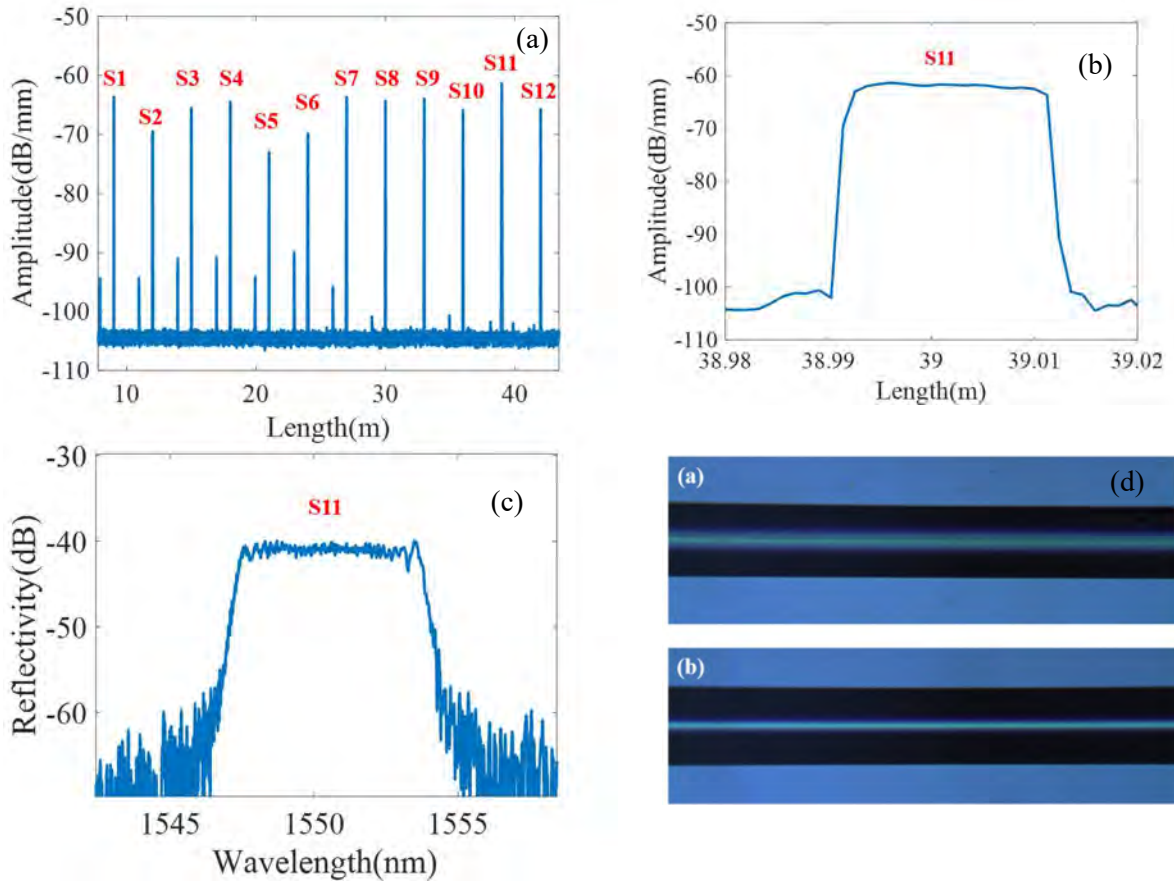
Figure 10. (a) Spatial profile of 12 fiber sensors fabricated by KrF 248-nm excimer laser through a phase mask; (b) the detail spatial profile of Sensor S11; (c) spectrum of Sensor S11 fabricated by a 1 laser pulse at 110 mJ; and (d) optical microscope image showing no coating damage.

Figure 10(a) and Figure 10(b) shows the Rayleigh backscattering profile of 12 fiber sensors fabricated continuously along a single fiber without a noticeable optical loss. These fiber sensors are fabricated directly through a fiber polymer coating. Figure 10(c) shows a reflection spectrum of the sensing point, using a chirped phase mask, a 10 nm bandwidth reflection point were produced. Figure 10(d) shows SEM imaging of fiber coating surface, which reveal no material and coating damage. These exciting results show that a reel-to-reel sensor fabrication without the need for a fiber draw-tower is highly feasible!

3. FABRICATION, CHARACTERIZATION, AND OPTIMIZATION OF HIGH-TEMPERATURE STABLE FIBER SENSORS

Research efforts presented in the previous section provide a reel-to-reel approach to fabricate fiber sensors without a fiber draw-tower. However, this approach only produces stable long-term fiber sensors up to 100°C. In this section, we report our research efforts to use the femtosecond laser writing scheme to produce high-temperature stable distributed fiber sensors.

The femtosecond laser has emerged as a promising technique in the fabrication of fiber sensors, especially for use in harsh environments [1]. Random gratings induced by femtosecond laser direct writing have been reported to enhance the scattering signal for application in optical frequency domain reflectometry (OFDR)-based distributed temperature sensing. By varying either the fiber writing speed or the laser repetition rate, random gratings can be generated to increase the sensing accuracy [2, 3]. However, the random grating with an ultra-low-loss [2] was generated by the femtosecond laser-induced homogeneous refractive index change (Type-I-fs), and thus, is not suitable for long-term monitoring of a temperature range larger than 500°C [4, 5]. Meanwhile, at a higher inscription pulse energy, another femtosecond laser-material interaction regime takes place, characterized by the formation of high-temperature stable nanostructures (Type-II-fs) [5-7] that have exhibited exceptional harsh environment endurance over 1000°C [8]. First observed in 2003, the femtosecond laser-induced nanograting is widely used for femtosecond laser selective etching for microfluidic channels [9] and FBGs for harsh environment applications [10, 11]. Recently, high-temperature stable sensors that exploit femtosecond laser-induced nanograting as Rayleigh scattering centers were tested in a reactive hydrogen gas environment with temperatures up to 800°C. The Rayleigh enhanced section has proven to be functional in both nuclear reactor cores [12] and internal to solid oxide fuel cells [13]. However, the sensors suffer from high propagation loss of 0.15 dB/cm; thus, the sensing range is limited.

In this report, we present a reel-to-reel femtosecond laser direct writing technique to inscribe Rayleigh scattering centers that are low-loss and thermally stable at high temperatures up to 1000°C in optical fiber cores for OFDR-based distributed temperature sensing. We found that by precisely tuning the laser exposure conditions, a signal-to-noise ratio (SNR) enhancement between 35–55 dB in Rayleigh backscattering signal and low propagation loss of 0.01 dB/cm was achieved. Cross-section morphology was observed under SEM to reveal the correlation between Rayleigh enhancement and the morphology of laser-induced nanograting formed in-fiber cores. Using a reel-to-reel setup, meters of Rayleigh enhancement were conveniently fabricated in the core of single-mode silica optical fiber for distributed fiber sensors, demonstrating improved thermal stability, SNR, and measurement resolution.

3.1 Femtosecond Laser Sensor Fabrications

A coherent Ti:sapphire regenerative femtosecond laser system was used for fiber sensor fabrication, focusing 800 nm, 270 fs, and 250 kHz light through a 100X 1.25-NA oil-immersion objective. The spot of laser focus was aligned with the center of the optical fiber core with the help of a high-precision motorized stage (Aerotech ABL2000). To achieve continuous femtosecond laser inscription, the fiber was translated using a customized reel-to-reel setup at a constant speed. A laser beam is linearly polarized, with its direction of polarization perpendicular to the direction of fiber translation. The backscattering behavior of the fiber sample was probed using a commercial optical backscattering reflectometer (OBR) (Luna 4600), as illustrated schematically in Figure 11(a). An example of the OBR backscattering profile of a Rayleigh enhanced section that is over 3 meters long is presented in Figure 11(b).

For the reel-to-reel fabrication setup, a compact fiber mount made by a three-dimensional printer was used to maintain the laser focus spot in the center of the fiber core during continuous Rayleigh scattering center writing, as shown in Figure 11(c). Altogether a customized pulley system and a motorized rotation stage, the inscription of fiber sensor meters were enabled with a simple alignment procedure. Figure 11(d) shows the sideview of the Rayleigh enhanced section under the optical microscope, with a continuous

modification track in the center of the fiber core. Afterwards, the fiber was cleaved at the section of femtosecond laser modification to examine its cross-section morphology using the SEM. The SEM photo in Figure 11(e) shows the formation of a self-organized nanostructure with a sub-wavelength period at the fiber core, whose morphology is consistent with the previous observation of the femtosecond laser-induced self-organized nanograting that is high-temperature stable up to 1100°C [4, 14].

3.2　Nanograting Engineering
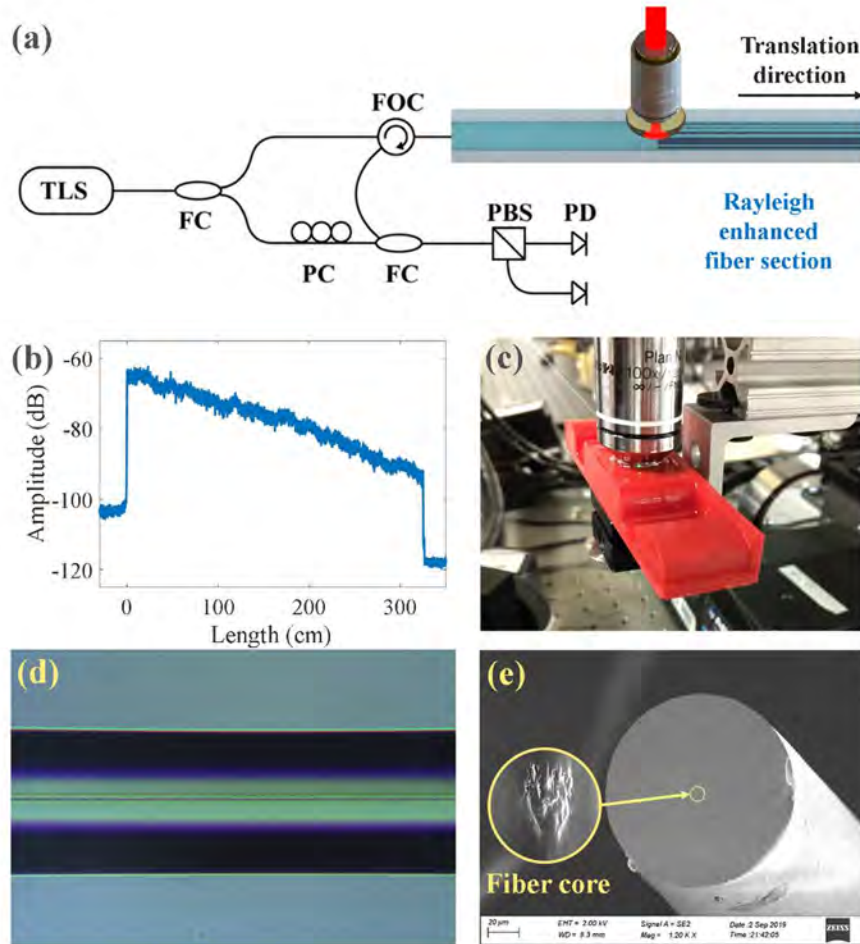
Figure 11. (a) Schematic of the fabrication setup; (b) the Rayleigh backscattering profile of a 325 cm Rayleigh enhanced section; (c) a photo of a segment of the reel-to-reel setup; (d) the microscopic photo of the fiber sideview; and (e) the SEM photo of the fiber cross-section, with the inset showing the zoomed-in image with nanograting in the fiber core.

SEM nanograting formation studies in correlation to the Rayleigh backscattering profile provide tell-tale clues on how to further optimize the fabrication process. Figure 12(a) through Figure 12(e) show the OBR-measured backscattering profiles of Rayleigh enhanced sections on a standard silica-core single-mode optical fiber (Corning SMF28e+) written with 160, 140, 120, 100, and 80 nJ inscription laser pulse energies at a constant speed of 0.5 mm/s, respectively, while their SEM photos in Figure 12(f) through Figure 12(j), respectively, revealed significant cross-section morphology variations in correlation to the OBR profiles. At a pulse energy below 60 nJ, no change in the Rayleigh backscattering profile could be measured, since the pulse energy is lower than the threshold of making Type I refractive index change in the fiber. At a pulse energy between 60 nJ and 100 nJ, an increase in the backscattering signal occurred, while there was

no visible morphology modification, as shown in Figure 12(j). This is the regime where the multiphoton absorption process induces a low-loss homogeneous refractive index modification, which is typically used to fabricate waveguides for integrated photonic circuit [6, 7]. The loss can be identified in Figure 12(e), where this can be explained by the localized refractive index change modification region with the size much smaller than the fiber core, resulting in a coupling loss due to the mismatch between the femtosecond laser-induced waveguide-like structure and the fundamental mode of the optical fiber. When pulse energy was higher than 100 nJ, an anisotropic nanostructure was observed in the fiber core, shown in Figure 12(f) through Figure 12(i), indicating the regime of laser-induced nanograting formation.
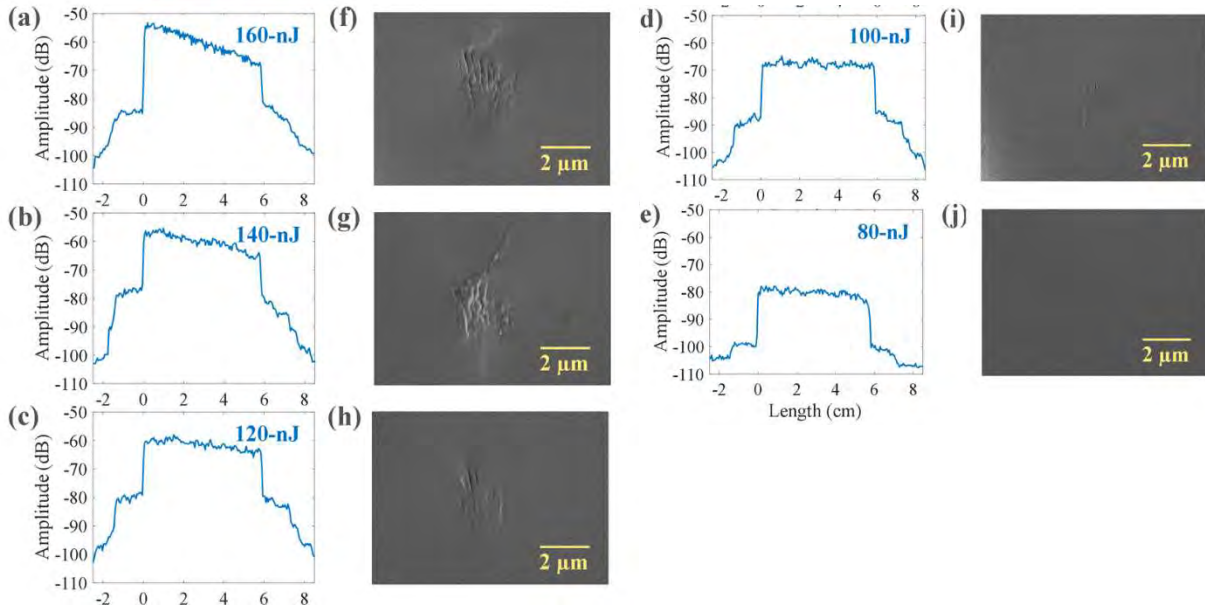
Figure 12. (a-e) Rayleigh backscattering profiles and (f-j) SEM photos of fiber core cross-section morphology of the Rayleigh enhanced sections fabricated using 160, 140, 120, 100, and 80 nJ pulse energies, respectively.

Figure 13 summarizes the dependence of OBR-measured propagation loss and SNR enhancement on the fabrication pulse energy at the pulse energies that allows the formation of high-temperature stable nanograting. The propagation loss is calculated from the linear fit of the optical OBR-measured return loss [15, 16], and the SNR enhancement is measured from the increase in returned backscattering signal of the Rayleigh enhanced fiber section as compared to the unmodified fiber section, where only intrinsic Rayleigh scattering exists [17]. A general relationship that is revealed from the OBR profile suggests that with an increase in laser pulse energy, both the SNR enhancement and the propagation loss increase. This is consistent with the SEM observations, as shown in Figure 12(f) through Figure 12(i), showing an increased size of the nanograting with increasing pulse energy [18, 19]. The controllability of loss and enhancement on pulse energy is a result of the distortion-free oil-immersion objective used during the fabrication process. Because of the high NA of the objective, the laser-induced nanograting size is much smaller than the size of the fiber core, and thus, the larger physical modification caused by nanograting increases the size of inhomogeneity inside the fiber core, resulting in a higher Rayleigh backscattering signal and scattering loss measured at the interrogator [24, 25]. As such, precise tuning of the Rayleigh enhanced section is enabled. By optimizing the conditions of laser exposure, the optimized exposure condition in SMF28e+ was found at 100-nJ, with a minimum loss of 0.01-dB/cm and an SNR enhancement of over 35-dB. This can be explained by the relatively small nanograting size formed at 100 nJ pulse energy, as seen in Figure 12(i), especially since 100 nJ is close to the threshold energy between the femtosecond laser-induced refractive index modification regime and the nanograting formation regime.
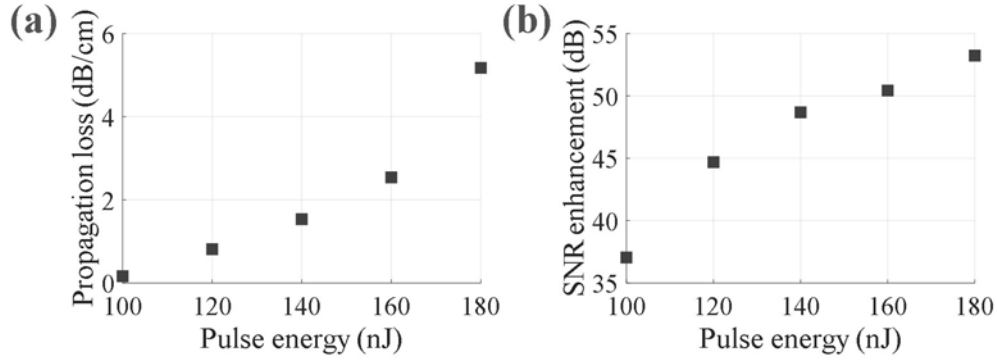
Figure 13. Dependence of (a) propagation loss, and (b) SNR enhancement on the exposure pulse energy.

Due to its asymmetric morphology, birefringence is introduced in optical fiber during the formation of nanograting. By simultaneously monitoring the two orthogonal s and p polarization states in the OBR-measured Rayleigh backscattering profile, the formation of nanograting can be identified using a non-invasive approach during fabrication [11, 17]. Figure 14(a) through Figure 14(d) show polarization states of the Rayleigh enhanced section written with a pulse energy of 140, 120, 100, and 80 nJ, respectively. No preference in polarization can be seen at 80 nJ, as seen in Figure 14(d), indicating the material modification is in the regime of isotropic positive refractive index change, consistent with the SEM observation in Figure 12(j). Meanwhile, as pulse energy reaches 100 nJ and beyond, beating occurs in the two polarizations. The birefringence of 140, 120, and 100 nJ profiles, observed in Figure 14(a) through Figure 14(c) were calculated to be 9.9×10-4, 2.7×10-4, and 0.8×10-4, respectively, which is due to the increased birefringent nanograting size, shown in Figure 12(g) through Figure 12(i). Compared to the low birefringence of ~10-7 for unmodified single-mode optical fiber (Corning SMF28e+), the scattering centers produce an approximate increase of three orders of magnitude in the in-fiber birefringence, which is consistent with previous descriptions of the in-fiber birefringence induced by nanograting [22, 23].
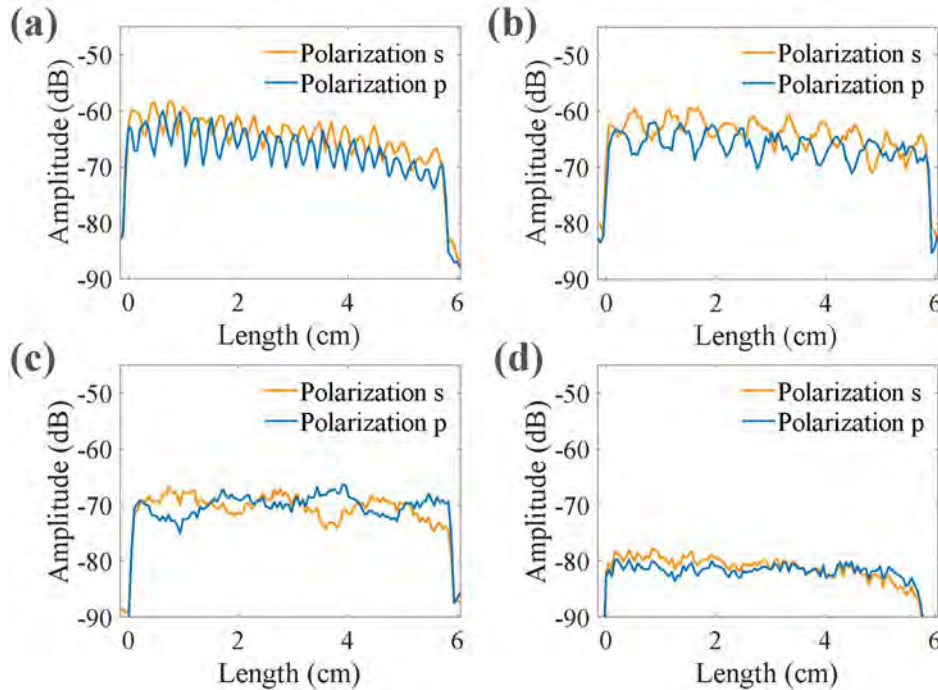
Figure 14. The s and p polarization states of the OBR-measured Rayleigh backscattering profiles, written with pulse energies of (a) 140 nJ, (b) 120 nJ, (c) 100 nJ, and (d) 80 nJ, respectively.

3.3   High-Temperature Performance

For high-temperature stability tests, a Rayleigh enhanced section fabricated with 100 nJ pulse energy and a 1 mm/s speed was first annealed at 1000°C for 20 hours and subjected to repeated heating and cooling cycles. Each cycle started from the ambient temperature, then rose to 1000°C at a rate of 5°C/min, remaining stable at each step of 100°C for 1 hour, followed by cooling at the natural rate from 1000°C back to the ambient. The temperature inside the box furnace was monitored with a Type-K thermocouple, and the Rayleigh enhanced sample was examined using the OBR every 10 minutes with 0.5 cm spatial resolution. Figure 15(a) shows the profile change right after fabrication, after annealing, and during each heating and cooling cycle. The characteristic curve for each cycle was calculated, as shown in Figure 15(b), as the sensitivity was measured to be -0.66 GHz/°C. The sensor was thermally stable throughout the temperature cycling with no obvious change in the backscattering profile. Afterwards, the Rayleigh enhanced section was kept at a constant temperature of 1000°C for 16 hours to verify the long-term thermal stability of the sensor. After 16 hours, it was still able to keep deriving correct temperature measurements from the Rayleigh enhanced section, using the ambient temperature profile as a reference, while the performance of the unmodified optical fiber degraded at 1000°C, as seen in Figure 15(c). This is probably due to the nanograting induced permanent physical modification exhibits better thermal stability at 1000°C than the intrinsic Rayleigh backscattering signal caused by inhomogeneities within the in-fiber core. Figure 15(d) represents the averaged spectral shift quality of both the Rayleigh enhanced fiber section and the unmodified fiber section over the time period of 16 hours at 1000°C, using the profile at the 0 hour at 1000°C as a reference. The range of spectral quality is a number between 0 and 1, which evaluates the quality of the cross-correlation in OFDR-based sensing [24, 45]. Overall, the Rayleigh enhanced section exhibited significantly improved high-temperature stability over a long-term.
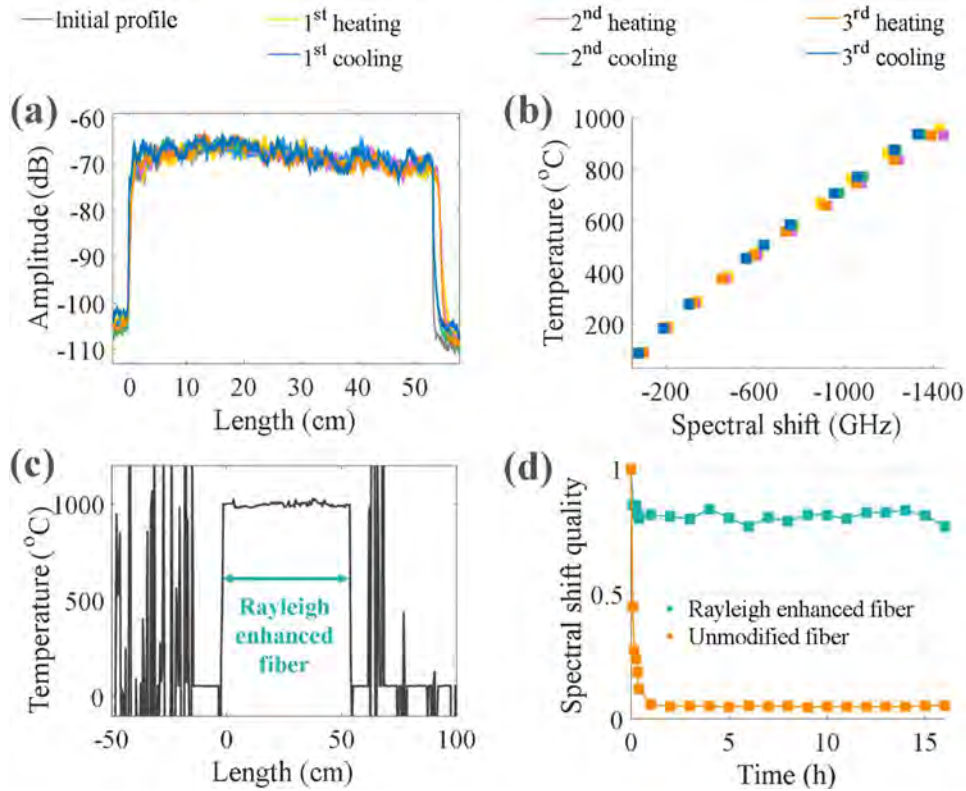
Figure 15. (a) The Rayleigh backscattering profile change; (b) the characterization curve during high-temperature test cycles; (c) the temperature measurement after three temperature cycles and 16 hours at 1000°C; and (d) the spectral shift quality change of the Rayleigh enhanced fiber section and unmodified fiber during 16 hours at 1000°C.

With a combination of laser exposure tuning and reel-to-reel fabrication, a 137 cm Rayleigh enhancement section was written with a 35 dB Rayleigh backscattering enhancement and a 0.01 dB/cm loss, as observed in Figure 16(a). The fiber sample was placed inside a thermally insolated container for 12 hours. Spectral shift quality of the Rayleigh enhanced section exhibits superior performance and the RMS (root mean square) noise was measured to be 0.012°C with a spatial resolution of 1 cm, which is about four times better than the unmodified sections measured to be at 0.054°C, as shown in Figure 16(b).
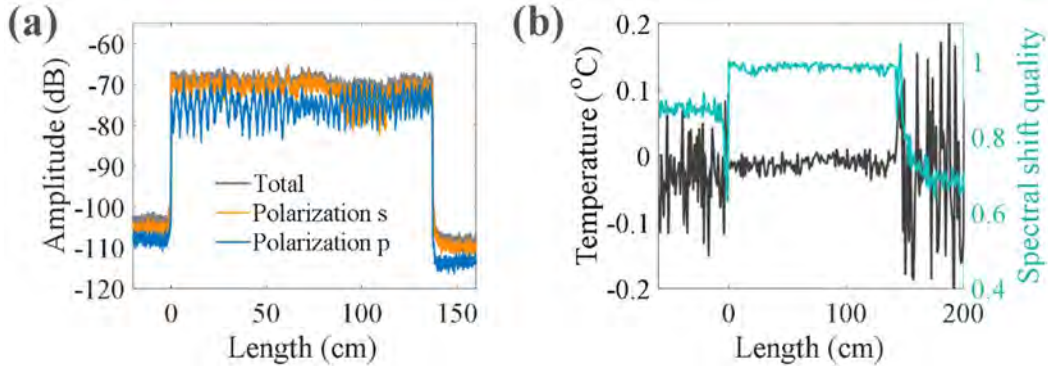
Figure 16. (a) The Rayleigh backscattering profile of a 137 cm Rayleigh enhanced section; and (b) the OBR-measured temperature variation (right) and spectral shift quality (left) at room temperature.

The fabrication process is highly flexible and can be used for other fiber geometries. The random airline-cladding (RAL) pure silica core optical fiber is a promising candidate for application in harsh environments. Compared to the commercial single-mode fibers with a Ge-doped silica fiber core, the RAL fiber is pure silica as with a cladding region composed of thousands of air holes [26, 27]. Similarly, continuous Rayleigh scattering centers were induced in RAL fiber and the propagation loss and SNR enhancement dependency on pulse energy were characterized in Figure 17(a). The pulse energy was increased to compensate for distortion of the laser focus from scattering in the random air hole cladding. Despite scattering at the RAL, the fabrication process was able to inscribe a highly localized modification area inside the fiber core with no damage to fiber cladding, as presented in the SEM photo in Figure 17(b).
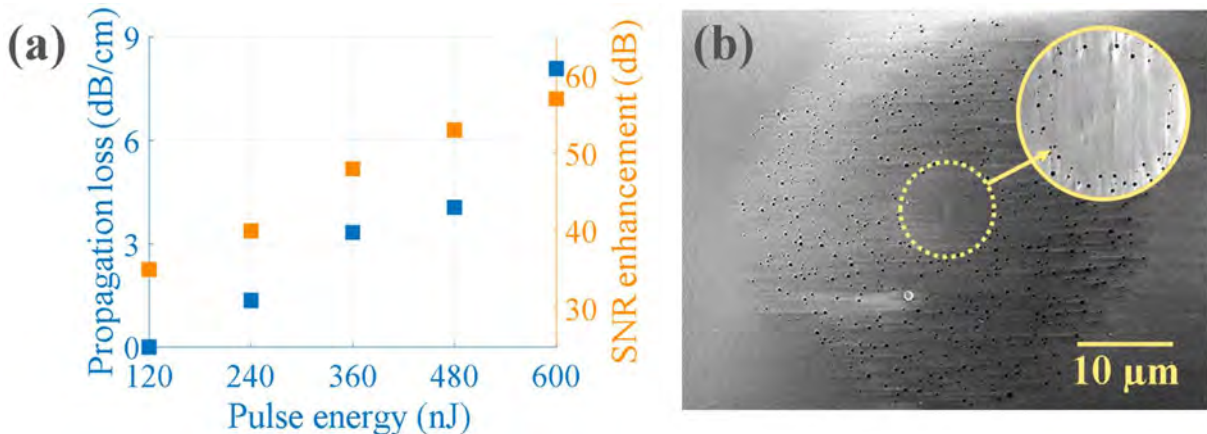
Figure 17. (a) Dependence of pulse energy and loss of Rayleigh enhanced section in RAL fiber; and (b) SEM photo of RAL fiber cross-section; inset is a zoomed-in image showing nanograting formation in the fiber core.

In summary, this part of the report presented a novel method of reel-to-reel femtosecond laser direct writing that enhances Rayleigh scattering on silica optical fiber for distributed temperature sensing. By studying the correlation between the Rayleigh scattering profile and the femtosecond laser-induced high-

19

temperature stable nanograting in-fiber core at the Rayleigh enhanced section, this section outlined a method to fine-tune the fabrication conditions to produce meters of optical fibers with an enhanced Rayleigh scattering profile and low propagation loss. We demonstrated improved high-temperature stability and SNR in repeated cycles for temperature up to 1000°C. Furthermore, by monitoring the birefringence, formation of high-temperature stable nanograting can be verified non-invasively. We also demonstrate the flexibility of the laser fabrication method in both standard telecommunication fiber and random airline-cladding fiber. The research presented herein opens powerful perspectives to fabricate high-quality and high-temperature stable optical fiber sensors with extended lengths for sensing applications in a harsh environment.

4. FIBER SENSOR ENABLED DISTRIBUTED ACOUSTIC SENSING AND DIGITAL TWIN MODELING

Research efforts presented in the previous sections provide two reel-to-reel approaches to fabricate fiber sensors without a fiber draw-tower. In this section, we detail our research efforts to apply these distributed fiber sensors for DAS for pipeline defect detection and classifications. This year's data harnessing and data analytics efforts consist of two aspects of efforts.

First, using distributed fiber sensors and a phase-sensitive optical time-domain reflectometry, we collected distributed acoustic data for both elbow and T-junctions. Using various simulated defects cut into the elbow and T-junctions, guided wave propagation and scattering of acoustic waves are collected along the pipe.

Second, stepping beyond last year's efforts, digital twin modeling using FEA was performed. Using ANSYS, a FEA simulation tool, we performed detailed numerical modeling of guided acoustic wave propagation in defective pipelines with elbow and T-junction structures. These simulation results have been compared with experimental data for mutual validation. Through both experimental data harness and numerical modeling, we aimed to use integrated data to train neural networks developed in Year 1 to improve the efficacy of artificial intelligence.

4.1. Phase-Sensitive Optical Time-Domain Reflectometry

Phase changes induced by vibration that is exerted on section fibers between two adjacent Rayleigh enhanced points can be captured and demodulated using a phase-sensitive optical time-domain reflectometry (ϕ-OTDR) system with a 3 × 3 coupler scheme. The demodulation system is shown schematically in Figure 18.

A 1550.12 nm laser light with a narrow bandwidth of 7 kHz is modulated to 20 ns pulses by a semiconductor optical amplifier (SOA). Then, the pulses are launched into a sensing fiber after being amplified by an erbium-doped fiber amplifier (EDFA). The backscattered pulses enter a branch of 3 × 3 coupler through an optical circulator. After splitting into three identical arms, two are reflected by Faraday rotator mirrors (FRMs). Since the optical paths difference of two FRMs matches the space between two adjacent Rayleigh enhanced points, the 3 × 3 coupler and the FRMs comprise a balanced Michelson interferometer. Reflected pulses sequentially form interferences, which would be captured by three photodetectors cooperating with a 250 MS/s data acquisition card. Finally, a LabVIEW program is used to process the interference signals. The phase from interference are extracted by a 3 × 3 demodulation algorithm. The principle of extraction is based on the intrinsic property of the 3 × 3 coupler that three outputs have a constant phase difference of 120°, which can be described as:

$$I_k = D + I_0 \cos[\phi(t) - (k-1)(2\pi/3)] \tag{4}$$

where k (k = 1, 2, 3) is the output number, D is the average of the output light intensity, and I_0 is the peak intensity of interference signals. The phase signals include phase shifts caused by signals to be detected and environmental noise. After processing by the demodulation algorithm, the output can be transformed to:

$$Vout = \sqrt{3}\phi(t) \tag{5}$$

The phase shifts caused by acoustic vibration are then quantitatively detected for further analysis.
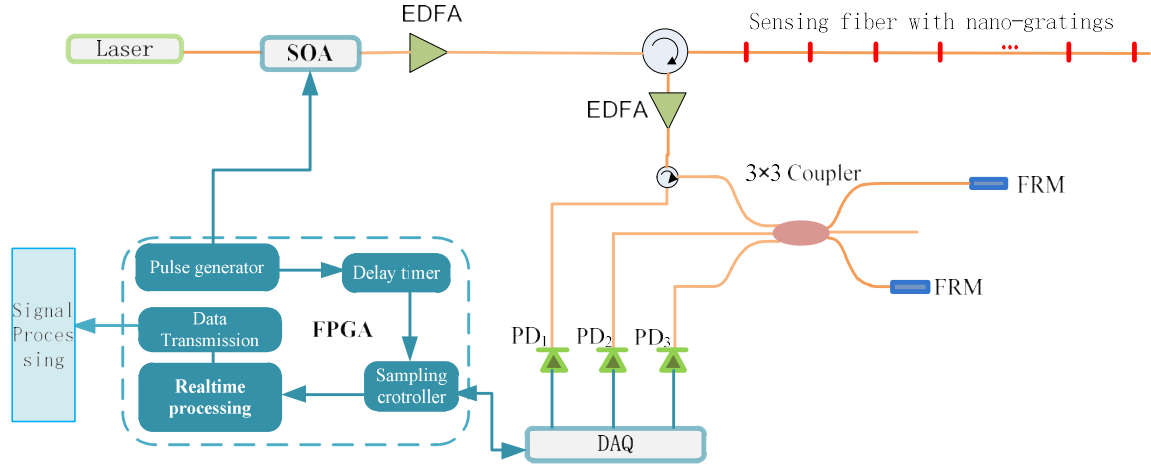
Figure 18. Schematic diagram of the φ-OTDR sensing system enhanced by ultrafast laser.

The DAS construction system used for data harness are mostly based on commercial off-the-shelf components. These includes an Er-doped fiber amplifier (EDFA), a semiconductor optical amplifier (SOA), photodetectors, and fiber components such as FRM and the data acquisition (DAQ) system. Most of the optoelectronic subsystems and fiber optical components are readily available at low costs, except the laser shown in Figure 18. However, the pulse generator used to drive SOA to produce short optical pulses for our DAS system are customer-developed by our group. A four-channel laser diode driver chip, LMH6526, contains two high-current outputs. This chip was designed for the laser control of a Blu-Ray DVD. It consists of two independent current channels with 300 mA capacity each. Both current channels were utilized to inject up to 600 mA current pulse into the SOA with less than a 1 ns raising time and 1 ns fall time. By dynamically selecting external resistors, the driver could determine the frequency and inject current amplitude of current pulse into SOA to produce the optical pulse for a DAS system. A thermoelectric cooler (TEC) controller ADN8831 was used to stabilize the temperature of SOA, which yield stability of current injection better than 2%. The duration of the current driving pulse can be controlled by an on-board field programmable gate array (FPGA) chip from 5 ns to 1 µs. The FPGA chip used in this PCB is XC6SLX9-2TQG144I. This corresponds to an interrogation spatial resolution of 50 cm up to 100 m. The developed PCB board also consists of several power sources to provide ±5 V output to power photodetectors and two EDFAs as shown previously in Figure 18. The delay timer is also included on-board.

4.2   Defect Detection of Pipe with Complex Shapes

The pipeline corrosion experiments based on the DAS system with the Rayleigh enhanced fiber was implemented in φ-OTDR scheme. In this fiscal year, we focused on the detection of defects on the pipe with complex shapes. This work focuses on elbow and T-junction defects. Using DAS, it offers the detection of acoustic waves along entire pipelines including a 90-degree elbow and a pipe network consisting of a T-junction. The low frequency responses of conventional data processing are ameliorated by changing to neural network machine learning. Both supervised and unsupervised methods have been implemented on signal post-processing.

Three techniques to discover how respective machine learning on various corrosions were studied. First, the convolutional neural network (CNN) without a tedious labeling issue was reviewed to confirm the feasibility of the system that resulted in as high as 94% recognition accuracy. Further, one with more

complicated factitious corrosion defects is for autoencoder due to its ability on finding relations inside the data themselves, which is closer to practical application because of unknown nature of defects. The unsupervised autoencoder achieved an overall accuracy of classification about 70% without any prior knowledge of defects. By connecting with a softmax layer at the output stage, the accuracy increases to 85% ultimately. The last experiment is designed to quantitively classify the defect depths by using machine learning. The accuracy can achieve 80% from the neural network.

By intentionally cutting V grooves inside the eight elbow connectors with linearly varying depths, which are from 0.1 to 0.8 cm and have a gradient of 0.1 cm, the experiment is designed to discover the relationship between defect depths and vibrations. As shown in Figure 19, all grooves share the same dimensions, except the depth. To excite acoustic vibrations, a hammer with a plastic head is adopted to strike one end of the pipeline at the frequency of ~5 Hz. S1~S7 denote seven optical fiber sensors formed by adjacent nano-gratings in the fiber core. They are tightly mounted on the steel pipes through UV curing. Correspondingly, there are also seven channels in the DAS system collecting data simultaneously. The sampling frequency of each channel is set to be 66.67 kHz, and a sampling period lasts 120 ms, which means 7990 sampling points could be acquired through one channel per cycle. The optical setup of the DAS is described in the next section.
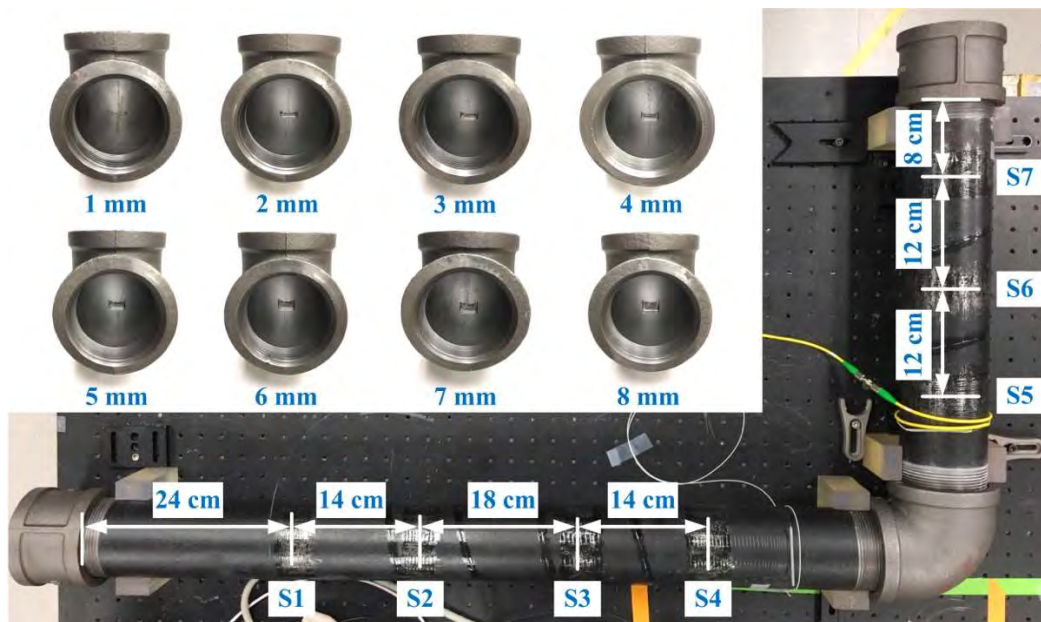
Figure 19. Experiment Setup. V Grooves with depths ranging from 0.1 to 0.8 cm, shown at the top of the figure, are cut on the inner surfaces of the elbows. Each elbow is mounted on a pipeline wired by seven optic sensors, and the excited vibration is respectively recorded.

The raw data collected from the experiment are stored in 11 LVM (LabView measurement file) files, one for each elbow used in the experiment. Each file contains multiple segments, one for every 120 ms of continuous acoustic recording. A total of 2894 effective segments, each containing one excitation on the elbow, were extracted. Each segment contains seven channels, one for each fiber sensor. Each channel contains 7990 data points, one for each sampling time. From these 7990 data points, 4890 data points representing the effective vibration (e.g., sampling index from 1551 to 6440, about 73ms of duration) were extracted, as shown in Table 2.

Table 2. Collected data in numbers for elbow structures.

Number of elbows	11
Number of defect depths	9
Number of sensors	7
Number of effective samples per segment per sensor	4890
Number of total effective segments	2894
Duration of each segment	120 ms

To ease the computational burden, each segment is low-pass-filtered at the 200th frequency component (~3.3kHz), then downsampled from 4890 to 399 sample points per segment per sensor. We can see from Figure 20 that the downsampling results in loss of information to some extent, but the overall characteristics of the signal are retained. To proceed with regression analysis, the data from each segment (e.g., 7 sensors x 399 sample points) are stacked as a vector of size 2793, respectively, and are labeled by the defect depth of the corresponding elbow.
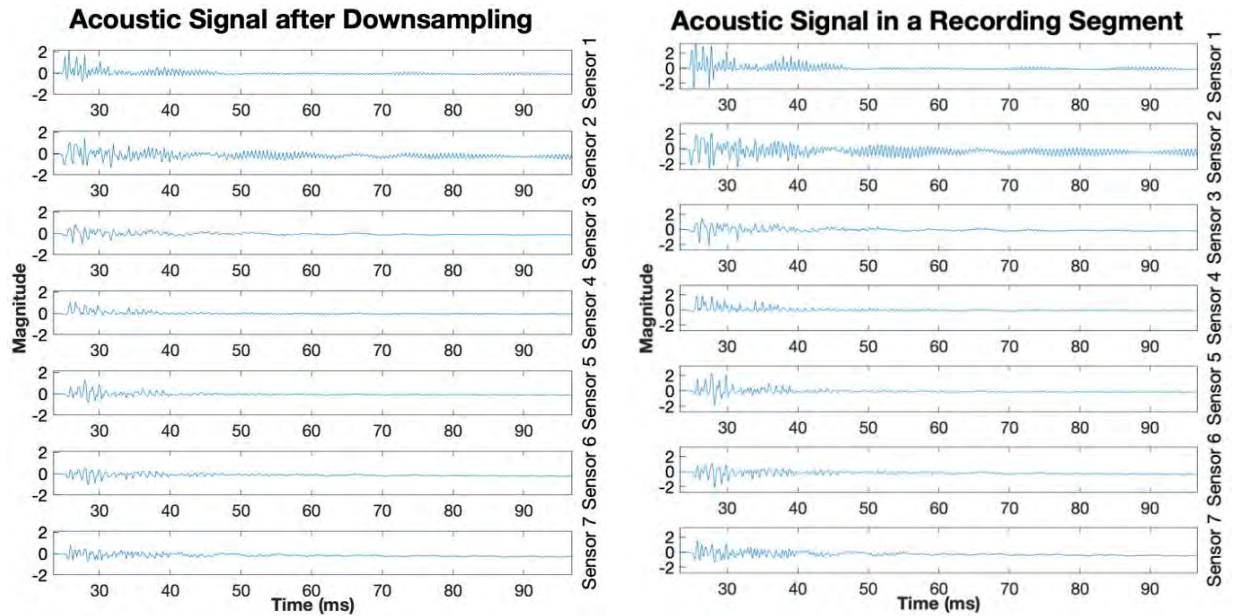
Figure 20. A typical segment of the data before (left) and after (right) downsampling.

In addition to elbow structures, acoustic data has also been collected for pipe structures with defected T-junctions. As another commonly used pipe joint structure, the T-junction provides another interesting structure, which diverts an acoustic signal to two different paths, as shown in Figure 21. For pipe structures joined by a T-junction, 11 fiber acoustic sensors are attached to three straight sections connected by a T-junction. Spacing between adjacent fiber sensors are separated by 150 mm on the straight section. Spacing between adjacent fiber sensors are separated by 80 mm on the straight pipe connected vertically to the other two sections. Six T-junctions were used for experiments. These include a T-junction without defects (e.g., a pristine sample). A V-grove with a length of 1.5 cm and depths of 1 mm, 2 mm, 3 mm, 4 mm, 5 mm, and 5.5 mm, respectively, was cut into the T-junction, as shown in an inset of Figure 21.
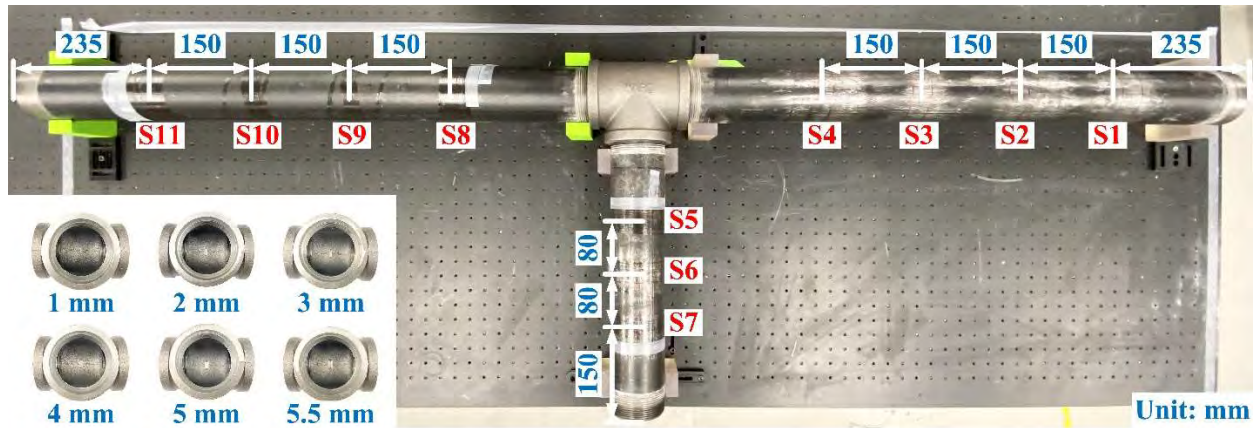
Figure 21. Experiment Setup. V Grooves with depths ranging from 1 to 5.5 mm are cut on the inner surfaces of the T connectors, shown at the bottom. Each connector is mounted on a pipeline wired by eleven optic sensors, and the excited vibration is respectively recorded.

Figure 22 shows typical acoustic data harnessed by 11 fiber sensors (left) and filtered data (right). The sensor data shown in Figure 22 show distinct different characteristics from that harnessed by the elbow structures. The strongest signal was harnessed by Sensor 4, possibly due to constructive interference from backscattered wave from both pipes connected to two output ports of the T-junction. Data harnessed Sensor 5-11 shows how acoustic wave propagated through two output ports. Majority of acoustic energy passes through the T-junction to the output pipe connected to the straight output port of the T-junction. Guided acoustic waves propagated through the pipe connected to the port that is 90° to the input port attenuates rapidly.
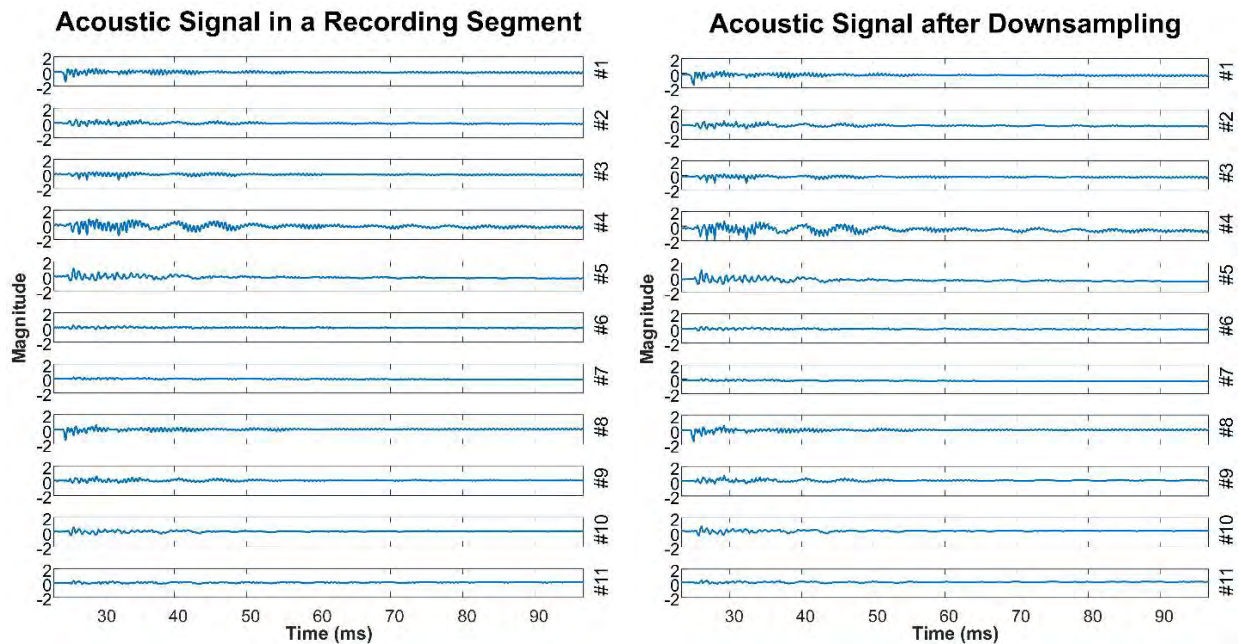
Figure 22. A typical segment of the data before (left) and after (right) downsampling.

4.3   Finite Element Analysis Digital Twin Modeling

To gain more insight on acoustic data harnessed by a distributed acoustic fiber sensor, FEA modeling was carried out this year to study how a guided acoustic wave is propagated through pipe structures with both elbow and T-junctions. This FEA simulations help us to reveal how various defects can impact guided acoustic wave propagation. By intentionally cutting V grooves inside eight elbow connectors with linearly varying depths, which are from 0.1 to 0.8 cm and have a gradient of 0.1 cm, the experiment described in Section 4.2 was designed to study the relationship between defect depths and vibrations.
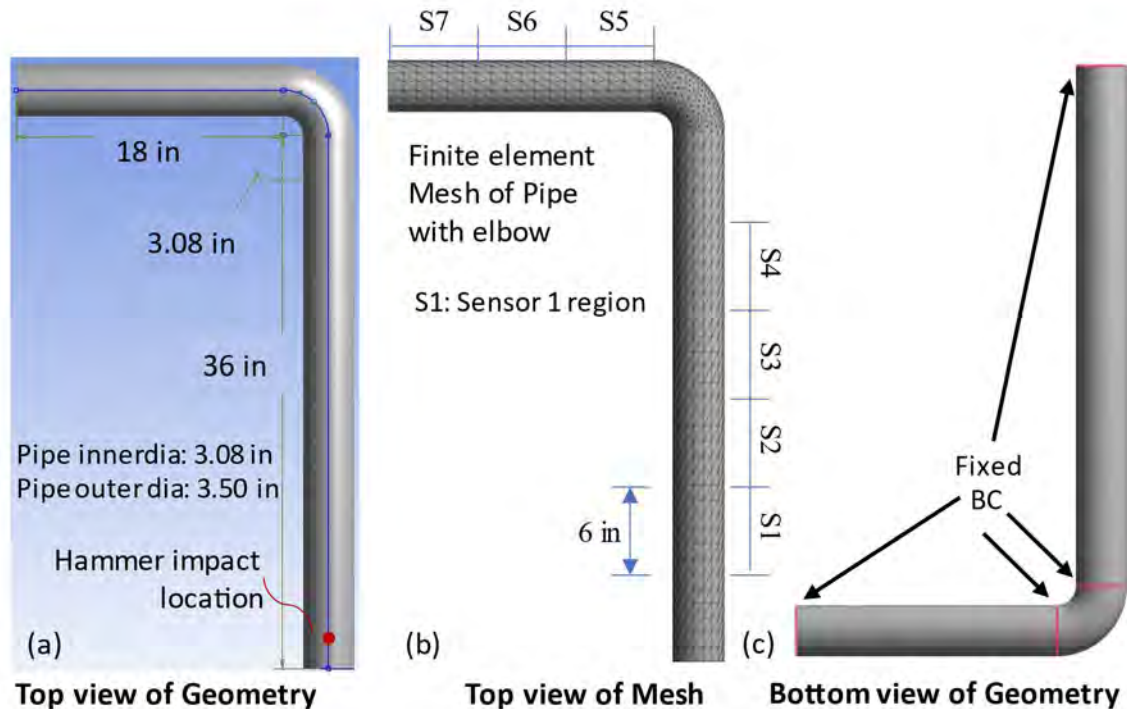
Figure 23. Inputs (e.g., geometry, mesh, and boundary conditions) to the finite element model.

Objectives of this FEA simulation are to develop a physics-based model to simulate sensor response of a pipeline instrumented with a DAS system and study the sensitivity of DAS response to intrinsic corrosion defects. In this section, transient structural analysis using finite element modeling was carried out to study response of fiber sensors. The geometry of the pipeline setup (including two pipes connected with a right-angle elbow) was modeled as a single three-dimensional body with the dimensions specified in Figure 23(a). The finite element mesh was obtained using quadrilateral tetrahedral elements, as depicted in Figure 23(b). The finite element model was constrained at the highlighted regions, as shown in Figure 23(c). Mechanical properties associated with structural steel were assigned to the finite element model. This model will be referred to hereafter as the *FE-Healthy* model. Modal analysis was conducted to determine the natural frequencies of the *FE-Healthy* model. Next, a square wave of amplitude 1000 N and a time duration of 4 ms was prescribed at the highlighted region in Figure 23(a) to model a hammer impact. The structural response of the *FE-Healthy* model corresponding to the impact was obtained using a transient structural analysis. Next, the geometry depicted in Figure 23(a) was modified to include a trench defect at the elbow with prescribed dimensions (e.g., depth – 0.1 in × length – 1.43 in × width – 1.1 in). The finite element model of the damaged pipeline, referred to hereafter as FE damaged, was developed using the same data as the *FE-Healthy* model. The simulated DAS response of each of the sensors were computed as the average circumferential strain rate across each region as shown in Figure 23(b).

FEA simulations were first carried out to study nature frequency of pipe structures with and without defects. These results are compared in Figure 24. It is evident from Figure 24 that the damaged natural frequencies show negligible deviation from healthy natural frequencies. This is consistent with the findings in literature that have noted that small local defects do not have a pronounced effect on the global natural frequencies.
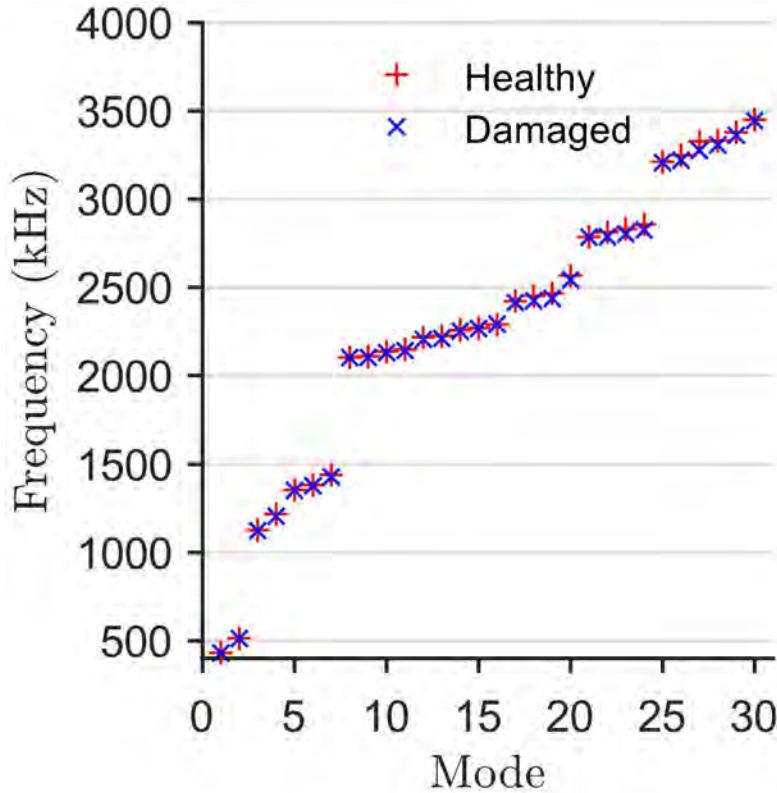
Figure 24. Healthy vs damaged natural frequencies of pipeline.

Figure 25 shows a comparison between simulated and experimental data generated on a defected elbow with a 5.5 mm deep trench. Excellent qualitative agreement between simulated and measured responses is seen in Figure 25. It is also evident that the elbow attenuates frequencies above 2 kHz as noted in the measurements. This is an important observation that suggested that fiber sensors with a low bandwidth can be used for pipeline inspection and defect classifications. These simulation datasets can be combined with experimental data harnessed by fiber sensors.

Recently, deep learning architectures (e.g. convolutional neural networks, autoencoders, etc.) have shown promise in classifying acoustic events based on the DAS measurements. It has also been shown that Fiber Optic Sensor (FOS) monitoring coupled with a Deep Neural Network (DNN) backed artificial intelligence engine can help detect intrinsic corrosion events in pipelines. However, a critical bottleneck to wide adoption of this technology is the availability of FOS data corresponding to the acoustic events of interest. It has been shown in literature that DNNs are prone to overfitting, unless they are trained on large datasets with a sufficient diversity of samples per class/event of interest. Extensive lab/field experimentation is necessary to meet this gigantic data acquisition task, which can be time-consuming, expensive, and impractical. However, this drawback can be mitigated by generating synthetic FOS data using physics-based simulation technologies. This approach can help generate FOS data corresponding to various acoustic events of interest at minimal cost.

26
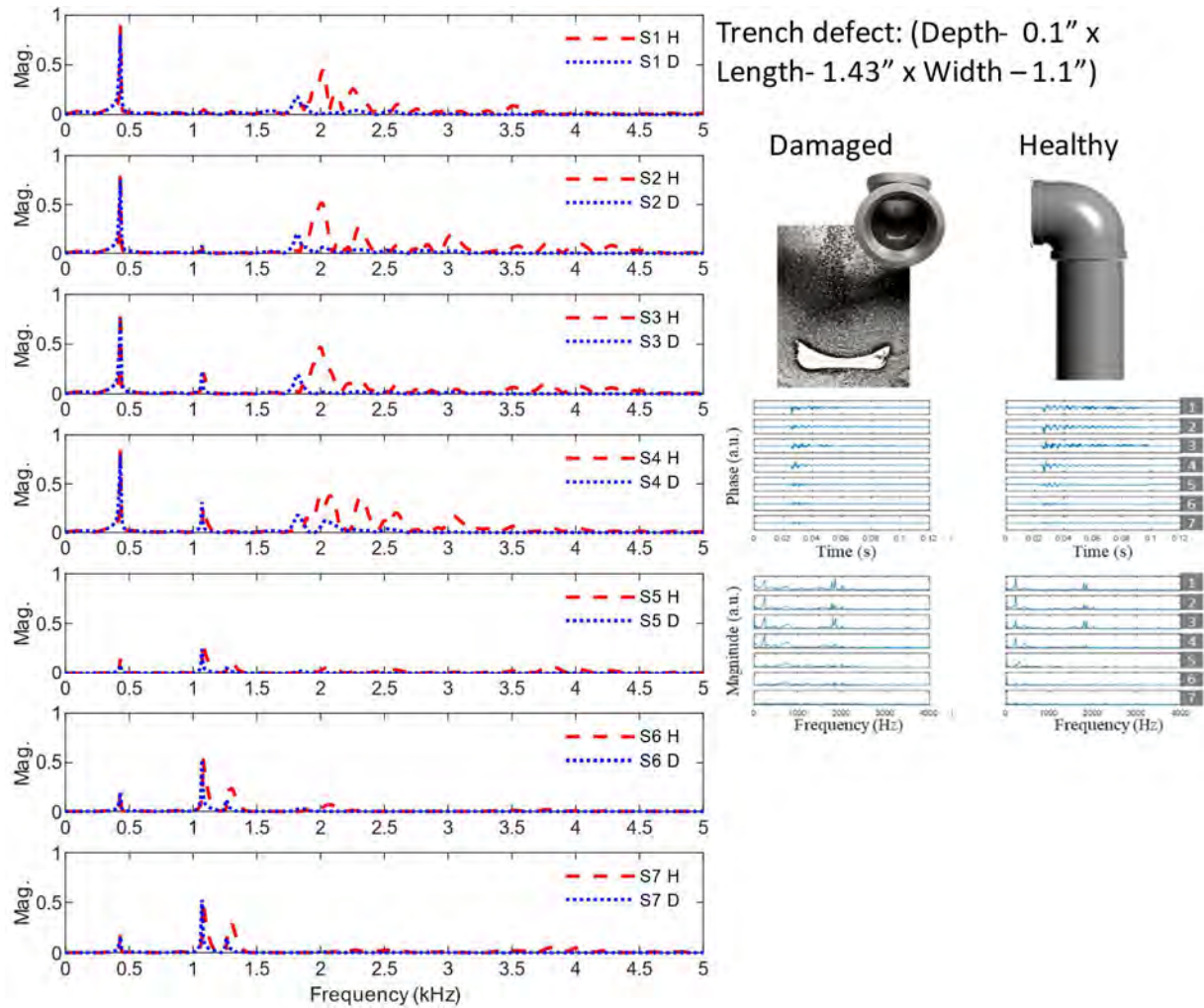
Figure 25. Simulated healthy vs damaged DAS responses.

Our FEA simulation studies were also carried out for pipe structures connected by a T-junction. This work develops a digital twin model to simulate FOS data obtained at various points on a pipeline assembly, as shown in Figure 26. The assembly consists of three pipes joined with a T-junction, as shown in Figure 26(a). Synthetic acoustic response data are generated corresponding to a healthy T-junction, as observed in Figure 26(b) vs. a T-junction with a 5.5 mm deep groove defect, seen in Figure 26(c). Further, the acoustic response to a hammer impact at two different locations, shown in Figure 26(d) and Figure 26(e) are generated and analyzed.

(a) Pipe Assembly: Three pipes joined with a T- junction.

(b) Healthy T-Junction.

(c) Groove defect (5.5 mm thickness).

(d) Sensor layout & hammer impact location A.

(e) Sensor layout & hammer impact location B.
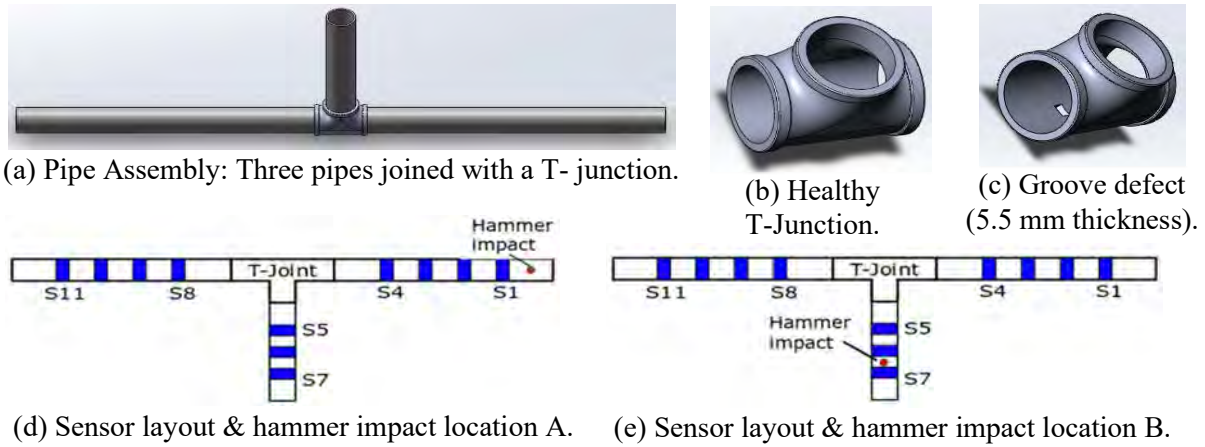
Figure 26. Pipeline assembly geometry, loading, and sensor configuration.

Digital Twin Model: A three-dimensional (3D) geometry of the pipeline assembly is designed using the manufacturer's specifications of the respective pipes and T-junction. The defect is introduced at the center of the junction to study the damaged acoustic response of the assembly. Next, the entire assembly is meshed using 3D solid tetrahedral elements. The junction is meshed, finely anticipating stress/strain concentrations at various sections. A transient structural analysis is carried out for a hammer impact loading (impact duration = 4 ms) and the maximum response at the various sensor locations are extracted for further examination.
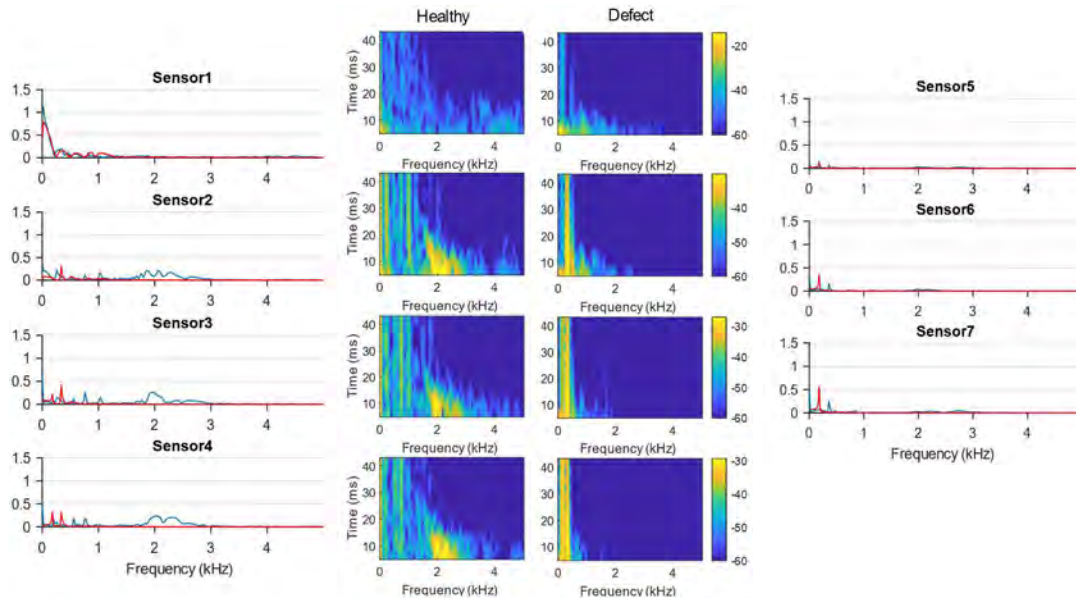
Figure 27. Fast fourier transform (FFT) and short time fourier transform (STFT) of maximum temporal strain profiles at various sensor location corresponding to the hammer impact loading location A (see Fig 1d). (-----) indicates damaged response while (----) indicates healthy response.

Results & Discussion: Use FFT and STFT to analyze the generated vibration signals. It is evident from Figure 27 that the acoustic response decays from sensors 1 to 4. Further, the acoustic response of the assembly with a healthy T-junction is primarily with two bandwiths (e.g., 0-1 kHz and 2-3 kHz). The high frequency response is attenuated by the damaged T-junction. This characteristic is again repeated in Figure 28, which corresponds to a different impact location.
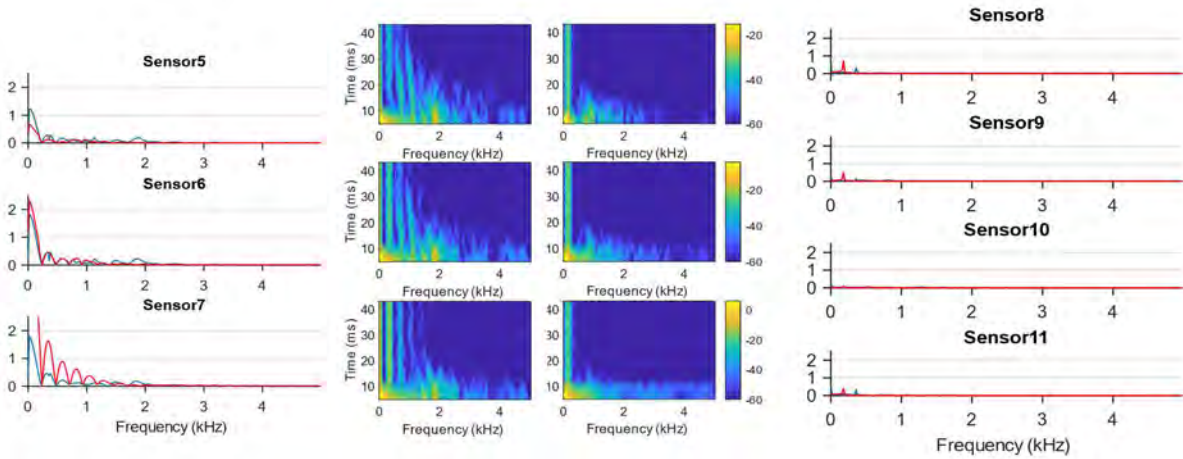
Figure 28. FFT and STFT of the maximum temporal strain profiles at various sensor location corresponding to the hammer impact loading location B, seen Figure 23(e).

Results presented in Figure 25, Figure 26, Figure 27, and Figure 28 show that the FEA simulation of transient responses of guided acoustic wave propagated in both elbow and T-junction structures show excellent agreement with experimental data. These simulation efforts suggested that the simulated data can be valuable to train the neural network. These comparison studies are particularly valuable given that there are a great variety of corrosive defects could be developed in pipeline. The use of simulated data will greatly accelerate training paces and prediction accuracy.

5. DEVELOPMENT OF LOW-COST ACOUSTIC SENSORS FOR PIPELINE MONITORING

Experimental and simulation studies carried out in Section 3 and Section 4 shows pipe structures with sharp bends, such as elbow and T-junctions, attenuate frequencies above 2 kHz as noted in the measurements. This is an important observation that suggested that fiber sensors with a low bandwidth can be used for pipeline inspection and defect classifications. In this section, we present our research efforts to develop Intrinsic Fabry-Perot Interferometer (IFPI) arrays for acoustic (or dynamic strain) measurements that can be interrogated using low-cost interrogation systems for an acoustic signal with a frequency less than 2 kHz.

5.1 Sensor Fabrication and Characterization

The fabrication of IFPI sensors are similar to those sensors fabricated for DAS. A standard telecom single-mode optical fiber (Corning SMF-28e+) was selected as the fiber platform for sensor fabrication. The single-mode fiber reel was mounted on a customized roll-to-roll fabrication setup for translation. The roll-to-roll setup is composed of a nano-precision motion stage, a rotary stage, an imaging system, 3-D printed parts, and mechanical pulleys, which enable precise inscription of sensors in a fiber core along an infinite distance with a simple alignment procedure. The fabrication process was done with a protective jacket to preserve the mechanical strength of the optical fiber. A Coherent RegA 9000 Ti:sapphire laser and amplifier system operating at 800 nm, 270 fs, and a 250 kHz repetition rate was used for fabrication. A linearly polarized laser beam was tightly focused inside the core of the fiber sample through a 100 × oil-immersion objective (Olympus 1-U2B235, NA 1.25) with index-matching oil to compensate for the aberration at the spherical fiber shape, shown in Figure 29(a). The input laser beam diameter is ~ 2 mm, which fills the rear aperture of the objective. Each FPI reflector was created by femtosecond laser pulses with 160 nJ on-target pulse energy. Figure 29(b) and Figure 29(c) show the cross-sectional view and side

view of an inscribed reflector, respectively. In this work, the length of a laser-induced reflector in-fiber core is 3 μm. This laser-modified cross-sectional area is approximately 2 μm by 2 μm, which is much smaller than the diameter of the fiber core (e.g., 8 μm). The reflectors appear black due to the random scattering of light caused by the physical modification at the laser focus spot inside the fiber core. A 630 nm red laser light was injected to observe the scattering feature of the reflectors, as observed in Figure 29(d). No physical modification could be identified except inside the fiber core, that is a distinct feature of the highly localized femtosecond laser-material interaction.
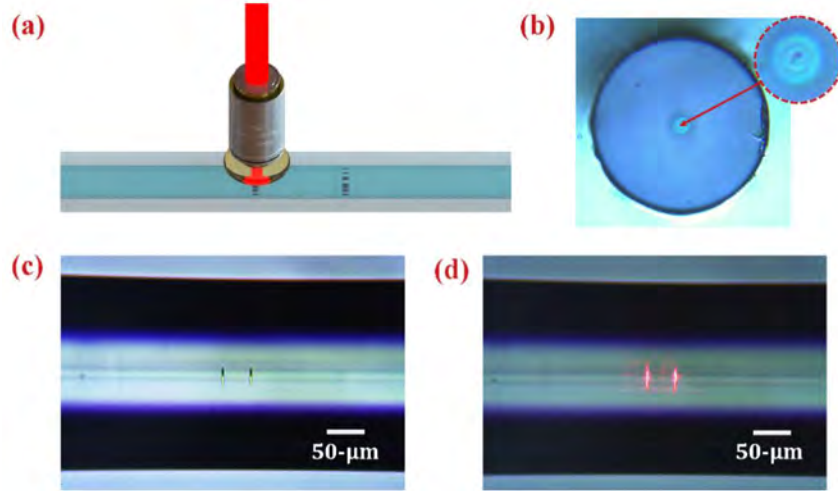
Figure 29. (a) Schematic of the IFPI fabrication setup; (b) the microscopic photo of the IFPI reflector cross-section; (c) microscopic photo of the IFPI side view of two nanograting reflectors; and (d) the scattering of red light at the reflectors.

The fabrication was characterized in real-time using a commercial Rayleigh scattering-based optical backscattering reflectometer (Luna OBR4600) to verify the location of the inscribed points. Figure 30(a) demonstrates the Rayleigh backscattering profile of an IFPI composed of a pair of laser-induced reflectors with a 1.3 mm cavity length. The femtosecond laser could induce a reflector with a 50 dB increase of the reflection signal above the intrinsic Rayleigh backscattering signal in a standard telecom fiber. After verification, a broadband method was used for IFPI characterization. Broadband light with a 60 nm bandwidth that ranged from 1510 to 1570 nm from a superluminescent light emitting diode (SLED) (EXS210059-01) was coupled to the IFPI fiber sample through a circulator. The interference fringes were detected by a 512-pixel Charge-coupled device CCD based spectrometer (Bayspec, FBGA) with a spectral range from 1510 to 1590 nm, as observed in Figure 30(b).
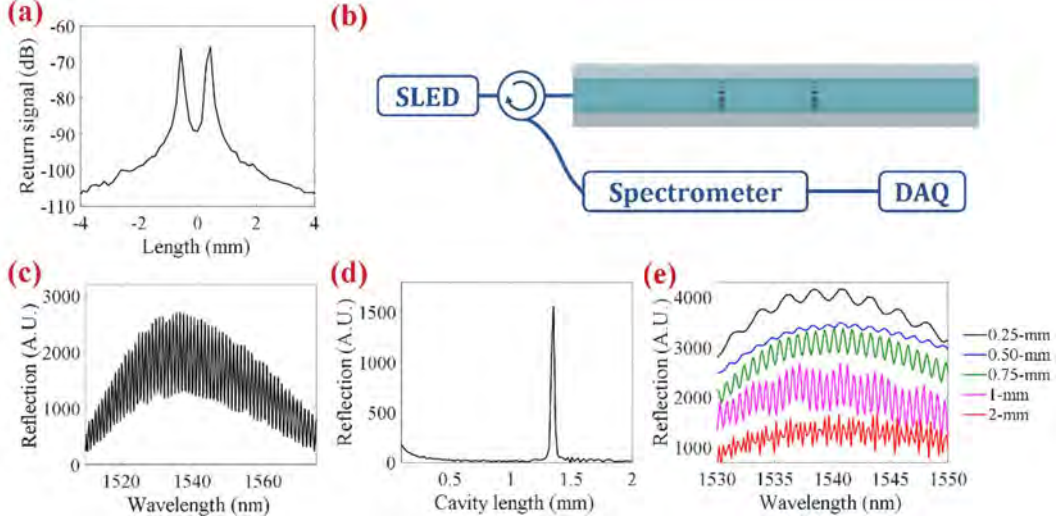
Figure 30. (a) Rayleigh backscattering profile of an IFPI using two nanograting reflectors; (b) setup of the IFPI demodulation system; (c) spectrum of a single IFPI cavity, (d) the FFT spatial domain; and (e) spectra of IFPIs with different cavity lengths.

Figure 30(c) shows the spectrum of a single IFPI. Assuming an identical reflection strength from the two reflectors, the interference spectrum of an IFPI can be expressed as a function of the wavevector, k:

$$I(k) = 2I_0(k)[1 + \gamma \cos(2k l_{OPD} + \varphi_0)] \tag{6}$$

where $I_0(k)$ is the reflection spectrum of the light source at the reflector, l_{OPD} is the optical path length (OPD) of the IFPI cavity, and γ is the fringe visibility. φ_0 is the phase delay of light that transmits through the first reflector, which is set to zero, since the length of the nanograting reflector of 3 μm is much shorter than the designed cavity lengths (e.g., between 250 to 2000 μm).

An increment in the OPD occurs with an increase in temperature, which can be expressed as:

$$\Delta l_{OPD} = 2(\frac{dn}{dT}l + \frac{dl}{dT}n)\Delta T = l_{OPD}(\alpha_o + \alpha_e)\Delta T \tag{7}$$

where α_0 is the thermo-optics coefficient of 8.6×10^{-6}/°C for the Ge-doped silica-core fiber, and α_e is the thermal expansion coefficient, equal to 0.55×10^{-6}/°C for silica fiber [30]. An FFT-based white light interferometry demodulation method was selected. Using non-zero-padded FFT with Buneman frequency estimation, the algorithm uses both the fringe order and phase information from a single spectrum to perform accurate absolute cavity length measurements of multiplexed IFPI devices [31-33]. The demodulated results for the 1.3 mm IFPI device presented in Figure 30(d) reveals that the cavity length is 1346.9 μm. The spectrum of IFPIs with different cavity lengths were demonstrated in Figure 30(e).

The experimental setup for vibration testing is shown in Figure 31. A SLED (EXS210059-01, Exalos) was used as a white light source with a 60 nm bandwidth (e.g., 1510 nm – 1570 nm). The broadband light emitted from the SLED passes through a circulator and is split into the REIFPI (Rayleigh enhanced intrinsic Fabry-Perot interferometers) sensor and the free-space FP(Fabry-Perot) cavity by a 50:50 optical coupler, respectively. The free-space FP cavity is built to measure the real-time displacement of the piezo stage in order to determine the absolute distance changes between two epoxy points [1]. This serves as a calibration to gauge the cavity length change measured by the REIFPI sensor. The backscattered interference light was then captured by a high-speed spectrometer (FBGA, Bayspec) with 512 pixels and 5 kHz maximum frame rate for demodulation. The frame rate of the spectrometer means the spectral acquisition rate. Two sides of

the REIFPI are glued between a stationary stage and a piezo-actuated stage using epoxy. The piezo-actuator was driven by a function generator at various frequencies.
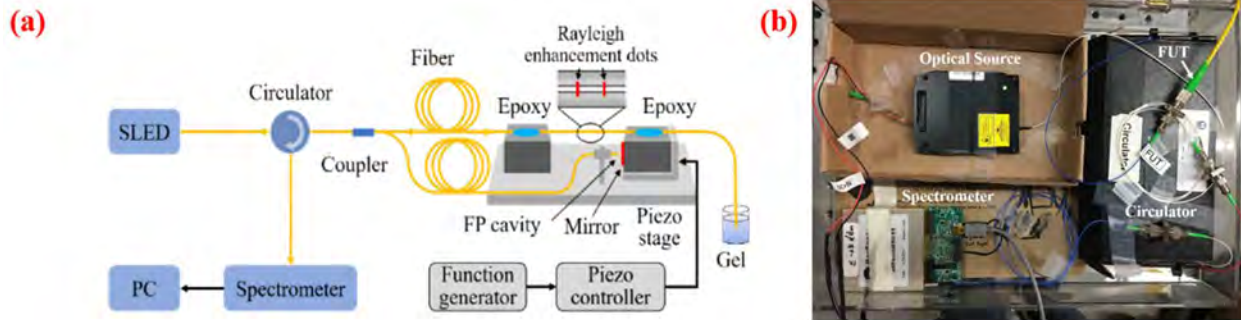

Figure 31. (a) Experimental setup of the vibration experiment; and (b) the picture of the sensor interrogation system.

5.2   Sensor Multiplexability and Dynamic Strain Testing

To test the high-temperature stability of femtosecond laser fabricated IFPI devices, a single IFPI sensor with a 1346.9 µm cavity length fabricated with a pulse energy of 160 nJ was placed inside a box furnace for temperature cycling. A formation of femtosecond laser-induced nanograting depends on the fabrication conditions, including pulse energy, pulse duration, and laser repetition rate. Results in our works were obtained using a femtosecond laser with a fixed pulse duration of 270 fs and a repetition rate of 250 kHz. SEM studies presented in Figure. 32(d-g) show that a pulse energy larger than 100 nJ is above the threshold of nanograting formation. This is consistent with laser processing conditions reported previously for nanograting formation in fused silica [42,43], which is the main composition of an optical fiber core. The backscattering profile, wavelength spectrum, and FFT spatial domain are presented in Figure 30(a), (c), and (d). The fiber sensor was first annealed at 1000°C for 5 hours, then went through repeated heating and cooling cycles. Each heating cycle started from room temperature, then raised to 1000°C in 100°C increments at a ramp rate of 5°C/min, and held at a steady temperature at each step of 100°C for 1 hour. The temperature of the furnace was continuously tracked using a type-K thermocouple with a USB temperature logger (Lascar EL-USB-LCD) every 20 seconds. Afterwards, the sample was cooled down in a furnace at a natural cooling rate. The cavity length was calculated with respect to the measurement from the electronic thermocouple to obtain the characterization curve in Figure 33(a). The sensitivity was 11.1 nm/ at a temperature below 300°C and was found to be 14.4 nm/°C at a temperature above 300°C – these measurements are similar to the behavior that was previously reported for high-temperature measurements for femtosecond laser-inscribed FBGs [48-51]. Figure 33(b) presents the measured FPI temperature against the thermocouple measurements, using the obtained characterization curve, and shows the precise sensor response of the IFPIs during repeated heating and cooling cycles.
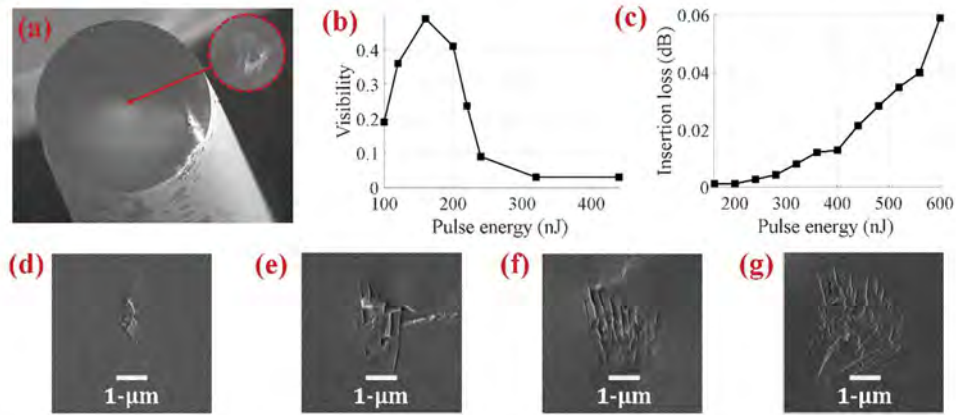
Figure 32. (a) SEM photo of the fiber cross-section where the IFPI was inscribed, inset shows the zoomed in fiber core area, (b) dependence of a 1-mm IFPI visibility on pulse energy, (c) dependence of the insertion loss per reflector on the pulse energy, and (d-g) the nanograting morphologies of the IFPI reflector in the fiber core area from overlapping pulses, inscribed with pulse energies of (d) 100-nJ, (e) 120-nJ, (f) 160-nJ, and (g) 200-nJ.
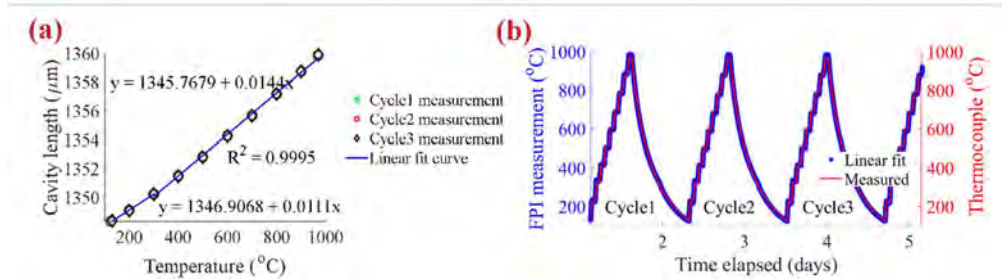

Figure 33. (a) Temperature response and linear fit curve of a single IFPI sensor; and (b) FPI measurement results and the thermocouple measurement during three repetitive heating cycles.

To characterize the crosstalk between multiplexed IFPI sensors interrogated with a single instrument, we fabricated two multiplexed IFPIs. A single-mode fiber was translated along the axial direction using a customized roll-to-roll writing setup to inscribe IFPI sensors at the points of interest. The optimized pulse energy of 160 nJ was used to achieve high fringe visibilities. Two IFPIs were inscribed with cavity lengths of 934.9 μm (Sensor 1) and 1050.2 μm (Sensor 2) respectively. Figure 34(a) shows the wavelength spectrum and demodulated results for the two-sensor array. Sensor 1 was placed under constant room temperature, while Sensor 2 was placed inside a tube furnace. The temperature of the furnace was increased from room temperature to 500°C. The cavity length change was demodulated in real-time. Figure 34(b) shows the relative cavity length change during two phases of the measurement process. The top subplot shows the measurement results when both IFPI sensors were kept at room temperature, while the bottom subplot shows when Sensor 2 was placed at 500°C and Sensor 1 was kept at room temperature. In the bottom subplot, the cavity length of Sensor 1 remained unchanged as Sensor 2 experienced an elongation of ~ 4720.2 nm as the ambient temperature rises to 500°C. The static test results shown in Figure 34(b) reveal minimal crosstalk between the two-sensor measurements. Fluctuations could also be identified from the results. Sensor 1 fluctuated at room temperature with a standard deviation of 0.0604 nm, corresponding to a temperature variation of ~ 0.007°C, as shown in the top portion of Figure 34(b). The cavity length of Sensor 2 fluctuated at 500°C with a standard deviation of 0.5722 nm, which corresponds to a temperature

33

fluctuation ~ 0.06°C, as shown in the bottom portion of Figure 34(b). This could be attributed to the fluctuation of the furnace temperatures.
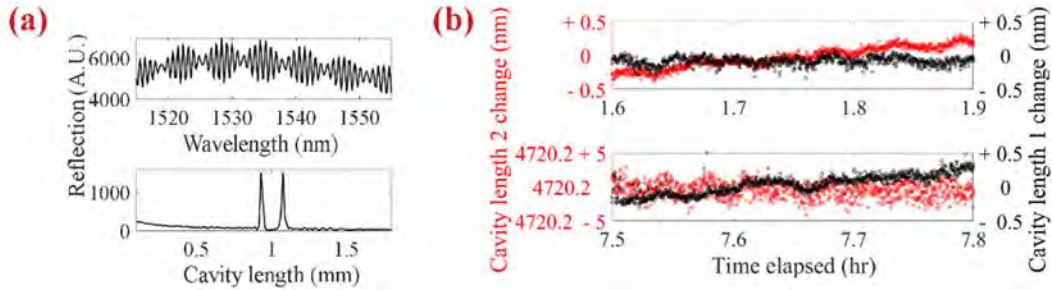

Figure 34. (a) Top portion: spectrum of the two multiplexed IFPIs. Bottom portion: the FFT of the IFPIs. (b) The cavity change of the IFPIs during the measurement when both Sensor 1 (black, right axis) and Sensor 2 (red, left axis) were placed at room temperature (top subplot) and when Sensor 1 stayed at room temperature while Sensor 2 was kept at 500°C (bottom subplot).

To demonstrate multiplexing capabilities, a string of six IFPI sensors were inscribed on a single-mode fiber sample using the roll-to-roll setup and 160 nJ pulse energy. Our crosstalk experiment in Figure 34 demonstrated that the sensor cavity length difference of 115 μm is sufficient to eliminate identifiable crosstalk between multiplexed sensors. As such, we inscribed a multiplexed IFPI array with the cavity lengths to be 398, 599, 888, 1190, 1527, and 1814 μm, respectively. A 1 cm spacing between two adjacent sensors was chosen in order to locate the IFPIs at different positions inside the box furnace. The interference fringe and FFT transformation of the 20 multiplexed sensors are shown in Figure 35(a) and Figure 35(b). The 20 IFPI peaks are highly distinguishable in the FFT domain. Even though the laser-modified cross-sectional area using 160 nJ pulse energy is much smaller than that of the fiber core, as shown in Fig. 32(f), the optical alignment to produce the nanograting in the center of the fiber core is still challenging to achieve.
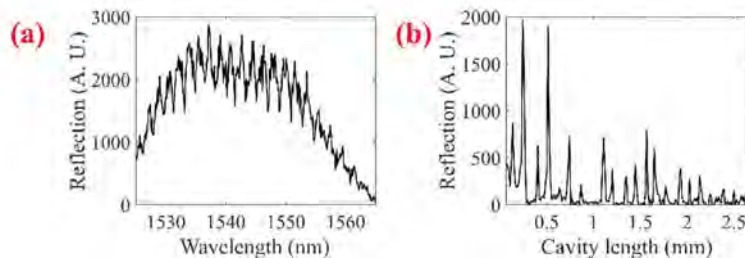
Figure 35. (a) spectrum of a multiplexed IFPI cavity; and (b) the FFT spatial domain of the spectrum.

In order to test the performance of the demodulation algorithm, two sensors with a cavity length of ~500 μm and ~1000 μm were tested when the spectral acquisition rates of spectrometer were set at 500 Hz, 1 kHz, 2 kHz, and 4 kHz, respectively. Figure 36 shows the static interference spectra of the ~1000 μm REIFPI sample at different spectrometer spectral acquisition rates. It is evident that the higher spectral acquisition rate corresponding to shorter integration time of the spectrometer yields worse fringe visibility. Figure 37(a) through Figure 37(d) show the demodulated static cavity lengths when the spectral acquisition rate of the spectrometer was set at 500 Hz, 1 kHz, 2 kHz, and 4 kHz, respectively. The standard deviations of the measurements were found to be 0.09 nm (92 nε), 0.2 nm (0.2 με), 0.4 nm (0.4 με), and 0.8 nm (0.8 με) from Figure 37(a) through Figure 37(d) at a lower spectrometer spectral acquisition rate, because the higher spectrometer integration time that leads to higher SNR. In addition, the standard deviations of the measurements descend with a higher SNR. Figure 37(e) shows the demodulated results on static measurements for the REIFPI with a cavity length of ~500 μm. At a 1 kHz spectral acquisition rate, the standard deviation is 0.034 nm (or 64 nε). From Figure 37, the real cavity lengths of the REIFPI samples

are ~530 μm and ~1000 μm, respectively. The deviation might be caused by the translation stage deviation when writing two defects in fabrication.
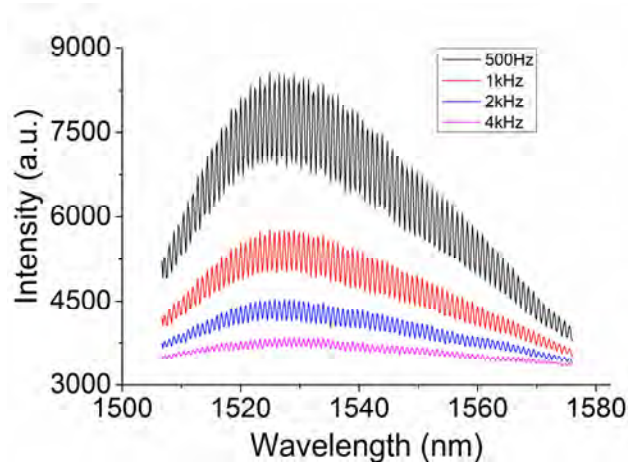
Figure 36. The interference spectra of the ~1000 μm REIFPI sample for 500 Hz, 1 kHz, 2 kHz, and 4 kHz spectral acquisition rates of spectrometer, respectively.
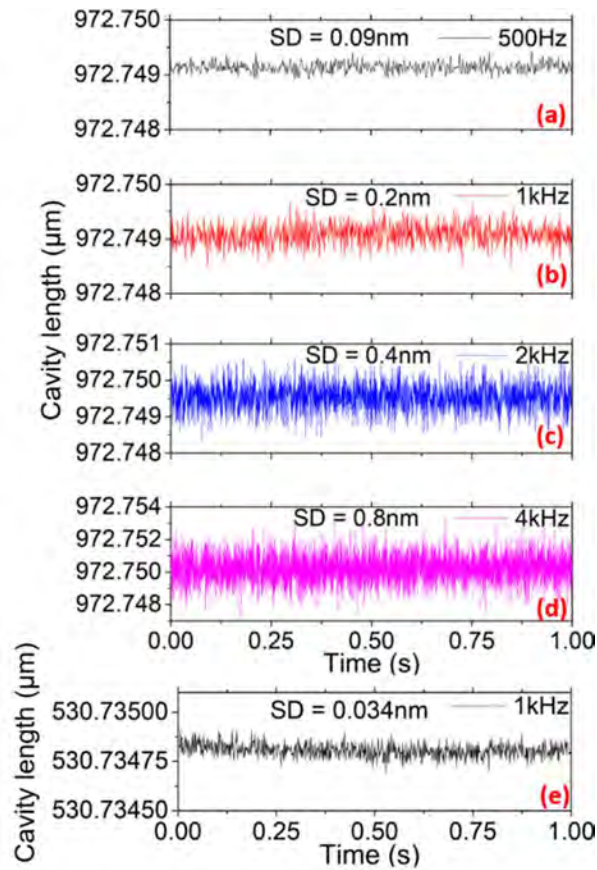
Figure 37. Static cavity length measurement results of the ~1000 μm REIFPI for the spectrometer spectral acquisition rates of (a) 500 Hz, (b) 1 kHz, (c) 2 kHz, and (d) 4 kHz, respectively. (e) Static cavity length measurements of another ~500 μm REIFPI sample at 1 kHz spectral acquisition rate.

5.3   Dynamic Strain Testing

The frequency response of the REIFPI sensor was also measured. The piezo stage was driven at vibration frequencies of 1 to 900 Hz and exerts dynamic strains to the ~1000-μm REIFPI sample. Figure 38 presents responsivity of REIFPI sensor at 10 Hz. A linear fitting was applied to the measured data in Figure 38. It reveals that the silica fiber strain measured by REIFPI sensor amounts to 68% of the strain induced by the piezo stage. The discrepancy between measured strain by REIFPI sensor and piezo-induced strain is likely due to the elasticity of the epoxy glue, which hampers strain transfer between the piezo stage and silica fiber.
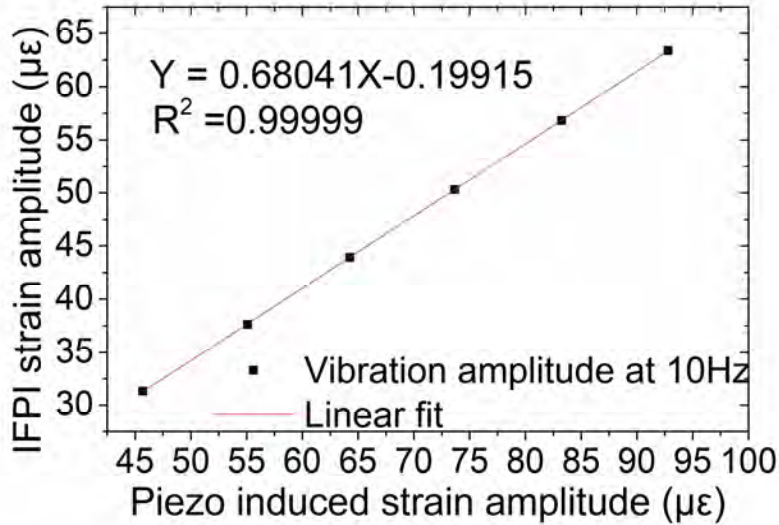
Figure 38. Linear fit of measured vibration strain amplitude of REIFPI sensor versus piezo-induced fiber strain amplitude at the vibration frequency of 10 Hz.

The strain responsivity in the frequency response was obtained from the slope of the linear fitting. The ~1000-μm REIFPI sample was tested for frequency response from 1 to 900 Hz shown in Figure 39. The frequency response curve is flat within the vibration frequency from 1 to 900 Hz, which can be used for vibration strain measurements.
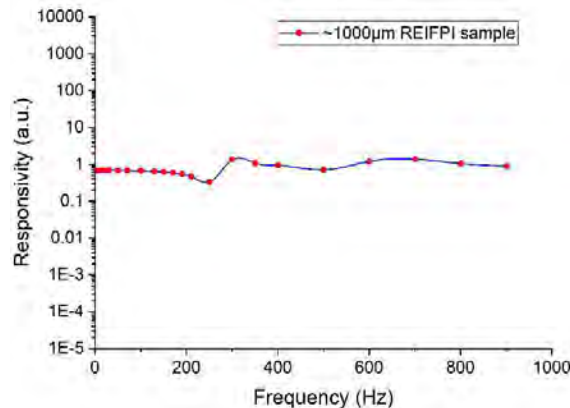
Figure 39. Frequency response of the REIFPI sensor within the vibration frequency from 1 to 900 Hz.

The performance of REIFPI sensor for vibration measurements also depends on the sensor interrogation systems. The time-domain vibration response of the REIFPI sensor was tested when the piezo stage

36

vibration amplitude was 7 με and frequencies were 30 Hz, 300 Hz, 500 Hz, and 900 Hz, respectively. The spectrometer spectral acquisition rate was 2 kHz. Figure 40(a) through Figure 40(d) show the measured vibration strain in time-domain by the REIFPI sensor at 30 Hz, 300 Hz, 500 Hz, and 900 Hz vibration frequency, respectively.
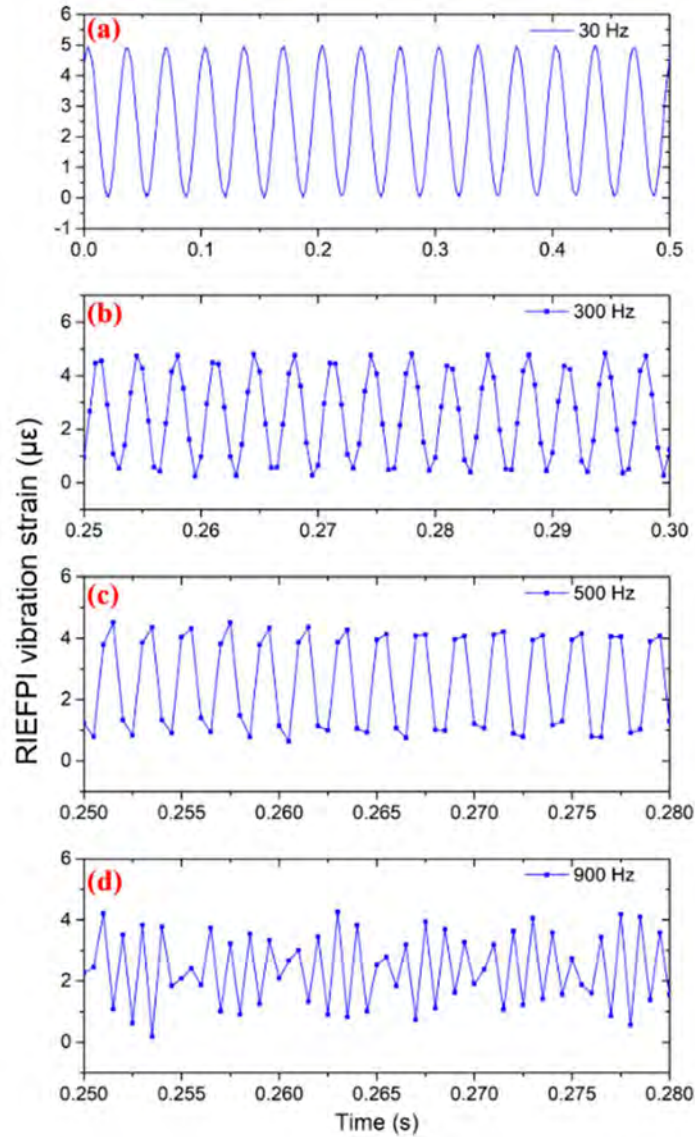
Figure 40. The vibration strain measured by the REIFPI sensor with a 2 kHz spectrometer spectral acquisition rate and a 7 με vibration strain amplitude of the piezo stage when the vibration frequencies are (a) 30 Hz, (b) 300 Hz, (c) 500 Hz, and (d) 900 Hz, respectively.

The minimum vibration strain amplitude detection was also characterized in detail when the piezo actuator was driven at 100 Hz. The vibration strain applied to the REIFPI sample with ~1000 μm cavity length was measured as shown in Figure 41(a). Frequency spectra of the measured vibration strain of the REIFPI cavity are shown in Figure 41(b) at the spectrometer spectral acquisition rates of 500 Hz, 1 kHz, 2 kHz, and 4kHz, respectively, when the piezo stage induced vibration strain amplitude is 55 με. Table 3 further details performance of the REIFPI vibration sensor for dynamic strain measurements at 100 Hz. It is evident that sensor sensitivity and measurement bandwidth of REIFPI sensor depends on how strong

37

Rayleigh backscattering is induced by the fs-laser. Table 3 shows the lower spectrometer spectral acquisition rate, the higher integration time, the higher SNR, and the lower minimum vibration strain amplitude detection. The minimum vibration strain amplitude detection is 27 nε/√Hz with 500 Hz spectral acquisition rate of the spectrometer. In this experiment, the bandwidth of vibration frequency is up to 2 kHz based on Nyquist theorem due to the maximum spectrometer spectral acquisition rate of 4 kHz.

Figure 41. (a) The measured vibration strain of the REIFPI cavity at 2 kHz spectral acquisition rates of spectrometer at 100 Hz vibration frequency; and (b) corresponding spectra spectrometer spectral acquisition rates of 500 Hz, 1 kHz, 2 kHz, and 4kHz, respectively.

Table 3. Minimum vibration strain amplitude measurement at the vibration frequency of 100 Hz for different spectral acquisition rates of spectrometer.

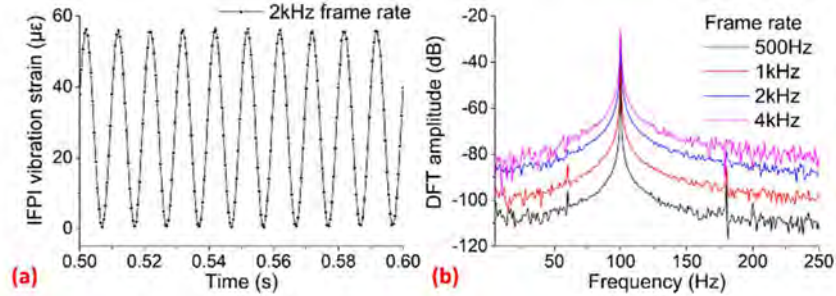| Spectral Acquisition Frequency	Integration Time (μs)	Measured DFT Peak Amplitude (dB)	Measured DFT Noise Floors (dB)	Minimum Vibration Strain (nε/√Hz)
500 Hz	1895	-43.7	-109.2	27
1 kHz	895	-37.4	-97.6	53
2 kHz	228	-31.5	-86.4	100
4 kHz	145	-25.6	-80.3	101

6. SUMMARY AND CONCLUSIONS

One of the primary challenges in ensuring safe and economically viable operation of NPPs is to develop cost-effective and robust CBM technology. However, after several decades of operations, NPPs have often evolved into unique, complex, and difficult systems for CBM implementation. This research report describes our effort in FY-19 and FY-20 to develop distributed fiber sensors that can withstand harsh NPP environments to develop distributed fiber sensors that can withstand harsh NPP environments to perform high spatial resolution active measurements for plant-scale monitoring. Data harnessed by fiber sensors were analyzed using various machine learning algorithm for defect detection and pipe health prognosis. Our research in FY-20 was primarily focused on the following four aspects:

- Working with Corning Inc., we have developed a new optical fiber that is suitable for reel-to-reel sensor fabrication without a fiber draw-tower facility. Using both femtosecond laser direct writing and KrF UV excimer laser fabrication schemes, fiber sensors are now produced in optical fiber without stripping polymer jackets. This effort represents a major advancement in distributed fiber sensor technology.

- To ensure the survivability of optical fiber sensors for NPP applications, our team carried out comprehensive laser writing optimization efforts and the evaluation of high-temperature fiber sensor stability. Through laser fabrication optimization tailored for a high-temperature environment, our

team demonstrated that ultra-low-loss fiber sensors can be fabricated to sustain a temperature of 800°C for long periods of times.

- Digital twin modeling, using FEA, our team performed detail numerical modeling of guided acoustic wave propagation in defective pipelines with elbow and T-junction structures. These simulation results have been compared with experimental data for mutual validation. Through both experimental data harness and numerical modeling, our team aims to use integrated data to train the neural networks developed in Year 1 to improve the efficacy of artificial intelligence.

- Through both the experimental and numerical modeling presented above, the frequency range of guided acoustic signal with significant propagation distance has been identified. Based on this knowledge, our team developed a low-cost distributed fiber sensor and interrogation system prototype that is suitable for field deployment. This work could significantly reduce the deployment cost of fiber sensors.

The greatest outcome of this year's efforts have yielded robust distributed fiber sensors that can be applied to a wide range of NPP components and systems for high spatial resolution data harness. The artificial intelligence big data analytics through deep learning using combined modeling and experimental data show potentials that extract critical information from sensor data even it is obscured by complex component shapes, structural aging, and variations due to sensor installation (e.g., human errors). The digital twin modeling provides solid groundwork to be completed in Year 3. The overall success will enable accurate prognosis of plant health and the development of effective CBM strategy. The success of this project will significantly reduce the operational cost, lower plant downtime, and improve compliance of regulatory requirements for nuclear and fossil fuel powered plants.

7. REFERENCES

[1] S. J. Mihailov, "Fiber Bragg grating sensors for harsh environments," Sensors, vol. 12, no. 2, pp. 1898-1918, Feb. 2012.

[2] P. Lu, S. Mihailov, D. Coulas, H. Ding, and X. Bao, "Low Loss Random Fiber Gratings Made with an fs-IR Laser for Distributed Fiber Sensing," J. Lightwave Technol., vol. 37, no. 18, pp. 4697-4702, Sep. 2019.

[3] Y. Xu, P. Lu, S. Gao, D. Xiang, S. Mihailov, and X. Bao, "Optical fiber random grating-based multiparameter sensor," Opt. Lett., vol. 40, no. 23, pp. 5514-5517, Dec. 2015.

[4] E. Bricchi, and P. G. Kazansky, "Extraordinary stability of anisotropic femtosecond direct-written structures embedded in silica glass," Appl. Phys. Lett., vol. 88, no. 11, pp. 111119, Mar. 2006.

[5] C. W. Smelser, S. J. Mihailov, and Dan Grobnic, "Formation of Type I-IR and Type II-IR gratings with an ultrafast IR laser and a phase mask," Opt. Express, vol. 13, no. 14, pp. 5377-5386, Jul. 2015.

[6] R. Osellame, et al., "Femtosecond laser micromachining: photonic and microfluidic devices in transparent materials," in Applied Physics, vol.123. Berlin, Germany: Springer Science & Business Media, 2012.

[7] K. Itoh, W. Watanabe, S. Nolte, and C. B. Schaffer, "Ultrafast processes for bulk modification of transparent materials," MRS Bull, vol. 31, no. 8, pp. 620-625, Aug. 2016.

[8] D. Grobnic, C. W. Smelser, S. J. Mihailov, and R. B. Walker, "Long-term thermal stability tests at 1000° C of silica fibre Bragg gratings made with ultrafast laser radiation," MST, vol. 17, no. 5, pp. 1009, Apr. 2006.

[9] M. Haque, K. Lee, S. Ho, L. A. Fernandes, and P. R. Herman, "Chemical-assisted femtosecond laser writing of lab-in-fibers," LOC, vol. 14, no. 19, pp. 3817-3829, Jul. 2014.

[10] S. J. Mihailov, D. Grobnic, C. Hnatovsky, R. B. Walker, P. Lu, D. Coulas, and H. Ding, "Extreme environment sensing using femtosecond laser-inscribed fiber Bragg gratings," Sensor, vol. 17, no. 12, pp. 2909, Dec. 2017.

[11] C. Hnatovsky, D. Grobnic, D. Coulas, M. Barnes, and S. J. Mihailov, "Self-organized nanostructure formation during femtosecond-laser inscription of fiber Bragg gratings," Optics Letters, vol. 42, no. 3, pp. 399-402, Feb. 2017.

[12] M. Wang, M. Zaghloul, S. Huang, A. Yan, S. Li, R. Zou, P. Ohodnicki et al.. "Ultrafast Laser Enhanced Rayleigh Backscattering on Silica Fiber for Distributed Sensing under Harsh Environment," in CLEO: Applications and Technology, May 2018, pp. ATh3P-4.

[13] A. Yan, S. Huang, S. Li, R. Chen, P. Ohodnicki, M. Buric, S. Lee, M. Li, and K. P. Chen, "Distributed Optical Fiber Sensors with Ultrafast Laser Enhanced Rayleigh Backscattering Profiles for Real-Time Monitoring of Solid Oxide Fuel Cell Operations," Sci. Rep., vol. 7, no. 1, pp. 9360, Aug. 2017.

[14] R. Taylor, C. Hnatovsky, and E. Simova, "Applications of femtosecond laser-induced self-organized planar nanocracks inside fused silica glass," Laser Photonics Rev., vol. 2, no. 2, pp. 26-46, Apr. 2008.

[15] J. F. Bauters, M. J. R. Heck, D. John, D. Dai, M. Tien, J. S. Barton, A. Leinse, R. G. Heideman, D. J. Blumenthal, and J. E. Bowers, "Ultra-low-loss high-aspect-ratio Si 3 N 4 waveguides." Opt. Express, vol. 19, no. 4, pp. 3163-3174, Feb. 2011.

[16] S. Huang, M. Li, S. M. Garner, M. Li, and K. P. Chen, "Flexible photonic components in glass substrates," Opt. Express, vol. 23, no. 17, pp. 22532-22543, Aug. 2015.

[17] B. J. Soller, D. K. Gifford, M. S. Wolfe, and M. E. Froggatt, "High resolution optical frequency domain reflectometry for characterization of components and assemblies," Opt. Express, vol. 13, no. 2, pp. 666-674, Jan. 2005.

[18] Y. Liao, W. Pan, Y. Cui, L. Qiao, Y. Bellouard, K. Sugioka, and Y. Cheng, "Formation of in-volume nanogratings with sub-100-nm periods in glass by femtosecond laser irradiation," Opt. Lett., vol. 40, no. 15, pp. 3623-3626, Jul. 2015.

[19] M. Beresna, M. Gecevičius, and P. G. Kazansky, "Polarization sensitive elements fabricated by femtosecond laser nanostructuring of glass," Opt. Mat. Express, vol. 1, no. 4, pp. 783-795, Aug. 2011.

[20] S. Eaton, W. Chen, H. Zhang, R. Iyer, J. Li, M. L. Ng, S. Ho, J. S. Aitchison, and P. R. Herman, "Spectral loss characterization of femtosecond laser written waveguides in glass with application to demultiplexing of 1300 and 1550 nm wavelengths," J. Lightwave Technol., vol. 27, no. 9, pp. 1079-1085, May. 2009.

[21] M. Ams, G. D. Marshall, and M. J. Withford, "Study of the influence of femtosecond laser polarisation on direct writing of waveguides", Opt. Express, vol. 14, no. 26, pp. 13158-13163, Dec. 2006.

[22] P. Lu, D. Grobnic, and S. J. Mihailov, "Characterization of the birefringence in fiber Bragg gratings fabricated with an ultrafast-infrared laser," J. Lightwave Technol., vol. 25, no. 3, pp. 779-786, Mar. 2007.

[23] L. A. Fernandes, J. R. Grenier, P. Marques, S. Aitchison, and P. R. Herman. "Strong birefringence tuning of optical waveguides with femtosecond laser irradiation of bulk fused silica and single mode fibers." J. Lightwave Technol., vol. 31, no. 22, pp. 3563-3569, Nov. 2013.

[24] M. Froggatt, and J. Moore, "High-spatial-resolution distributed strain measurement in optical fiber with Rayleigh scatter," Appl. Opt., vol. 37, no. 10, pp. 1735-1740, Apr. 1998.

[25] S. T. Kreger, A. K. Sang, D. K. Gifford, and M. E. Froggatt, "Distributed strain and temperature sensing in plastic optical fiber using Rayleigh scatter," In Fiber Optic Sensors and Applications VI, vol. 7316, pp. 73160A. SPIE, Apr. 2009.

[26] M. A. S. Zaghloul, M. Wang, S. Huang, C. Hnatovsky, D. Grobnic, S. Mihailov, M. Li et al, "Radiation resistant fiber Bragg grating in random air-line fibers for sensing applications in nuclear reactor cores," Opt. Express, vol. 26, no. 9, pp. 11775-11786, Apr. 2018.

[27] S. J. Mihailov, C. Hnatovsky, D. Grobnic, K. Chen, and M. Li, "Fabrication of bragg gratings in random air-line clad microstructured optical fiber," IEEE Photon. Technol. Lett., vol. 30, no. 2, pp. 209-212, Dec. 2017.

[28] Chen, T.; Wang, Q. Q.; Chen, R. Z.; Zhang, B. T.; Jewart, C.; Chen, K. P.; Maklad, M.; Swinehart, P. R., Distributed high-temperature pressure sensing using air-hole microstructural fibers. Optics Letters 2012, 37, (6), 1064-1066.

[29] Kim, K.; Zhang, S. J.; Salazar, G.; Jiang, X. N., Design, fabrication and characterization of high temperature piezoelectric vibration sensor using YCOB crystals. Sensor Actuat a-Phys 2012, 178, 40-48.

[30] A. Othonos, "Fiber bragg gratings," Rev. Sci. Instrum. 68(12), 4309-4341 (1997).

[31] Z. Yu and A. Wang, "Fast white light interferometry demodulation algorithm for low-finesse Fabry–Pérot sensors," IEEE Photon. Technol. Lett. 27 (8), 817-820 (2015).

[32] Z. Yu, and A. Wang, "Fast demodulation algorithm for multiplexed low-finesse Fabry–Perot interferometers," J. Lightwave Technol. 34(3), 1015-1019 (2016).

[33] Y. Yang, E. Wang, K. Chen, Z. Yu, and Q. Yu, "Fiber-optic Fabry–Perot sensor for simultaneous measurement of tilt angle and vibration acceleration," IEEE Sens. J. 19(6), 2162-2169 (2018).

[34] M. Beresna, M. Gecevičius, and P. G. Kazansky. "Ultrafast laser direct writing and nanostructuring in transparent materials," Adv. Opt. Photonics 6(3), 293-339 (2014).

[35] L. P. R. Ramirez, Matthias Heinrich, Sören Richter, Felix Dreisow, Robert Keil, Alexander V. Korovin, Ulf Peschel, Stefan Nolte, and Andreas Tünnermann. "Tuning the structural properties of femtosecond-laser-induced nanogratings." Appl. Phys. A 100(1), 1-6 (2010).

[36] C. W. Smelser, S. J. Mihailov, and Dan Grobnic, "Formation of Type I-IR and Type II-IR gratings with an ultrafast IR laser and a phase mask," Opt. Express 13(14), 5377-5386 (2005).

[37] C. Hnatovsky, D. Grobnic, D. Coulas, M. Barnes, and S. J. Mihailov, "Self-organized nanostructure formation during femtosecond-laser inscription of fiber Bragg gratings," Opt. Lett. 42(3), 399-402 (2017).

[38] S. Loranger, F. Parent, V. Lambin-Iezzi, and R. Kashyap, "Enhancement of Rayleigh scatter in optical fiber by simple UV treatment: an order of magnitude increase in distributed sensing sensitivity," in Opt. Components and Mat. XIII, SPIE 9744, 97440E (2016).

[39] P. G. Kazansky, H. Inouye, T. Mitsuyu, K. Miura, J. Qiu, K. Hirao, and F. Starrost. "Anomalous anisotropic light scattering in Ge-doped silica glass," PRL 82(10), 2199-2202 (1999).

[40] Y. Shimotsuma, P. G. Kazansky, J. Qiu, and K. Hirao, "Self-organized nanogratings in glass irradiated by ultrashort light pulses," PRL 91(24), 247405 (2003).

[41] M. Haque, K. Lee, S. Ho, L. A. Fernandes, and P. R. Herman, "Chemical-assisted femtosecond laser writing of lab-in-fibers," LOC 14(19), 3817-3829 (2014).

[42] C. Hnatovsky, R. S. Taylor, P. P. Rajeev, E. Simova, V. R. Bhardwaj, D. M. Rayner, and P. B. Corkum, "Pulse duration dependence of femtosecond-laser-fabricated nanogratings in fused silica," Appl. Phys. Lett. 87(1), 014104 (2005).

[43] S. Richter, M. Heinrich, S. Döring, A. Tünnermann, and S. Nolte, "Formation of femtosecond laser-induced nanogratings at high repetition rates," Appl. Phys. A 104(2), 503-507 (2011).

[44] S. Rajesh and Y. Bellouard, "Towards fast femtosecond laser micromachining of fused silica: The effect of deposited energy," Opt. Express 18(20), 21490-21497 (2010).

[45] A. Champion and Y.Bellouard, "Direct volume variation measurements in fused silica specimens exposed to femtosecond laser," Opt. Mater. Express 2(6), 789-798 (2012).

[46] Y. Zhang, Y. Li, T. Wei, X. Lan, Y. Huang, G. Chen, and H. Xiao, "Fringe visibility enhanced extrinsic Fabry–Perot interferometer using a graded index fiber collimator," IEEE Photonics J. 2(3), 469-481 (2010).

[47] Yang, Y.; Wang, E. Y.; Chen, K.; Yu, Z. H.; Yu, Q. X., Fiber-Optic Fabry-Perot Sensor for Simultaneous Measurement of Tilt Angle and Vibration Acceleration. Ieee Sensor Journal 2019, 19, (6), 2162-2169.

[48] J. Deng, D. N. Wang, and H. Zhang, "Femtosecond Laser Inscribed Multiple In-Fiber Reflection Mirrors for High-Temperature Sensing," J. Lightwave Technol. 37(21), 5537-5541 (2019).

[49] A. Yan, S. Huang, S. Li, R. Chen, P. Ohodnicki, M. Buric, S. Lee, M. Li, and K. P. Chen, "Distributed Optical Fiber Sensors with Ultrafast Laser Enhanced Rayleigh Backscattering Profiles for Real-Time Monitoring of Solid Oxide Fuel Cell Operations," Sci. Rep. 7(1), 1-9 (2017).

[50] R. Chen, A. Yan, M. Li, T. Chen, Q. Wang, J. Canning, K. Cook, and K. P. Chen, "Regenerated distributed Bragg reflector fiber lasers for high-temperature operation," Opt. Lett. 38(14), 2490-2492 (2013).

[51] T. Wang, L. Shao, J. Canning, and K. Cook, "Temperature and strain characterization of regenerated gratings," Opt. Lett. 38(3), 247-249 (2013).